

OPEN ACCESS

EDITED BY
Majid Jabir,
University of Technology, Iraq

REVIEWED BY
Shivani R. Pandya,
Narnarayan Shastri Institute of Technology,
India
Vijaya Parthasarathy,
Bharathiar University, India

RECEIVED 01 August 2025 REVISED 22 September 2025 ACCEPTED 27 October 2025 PUBLISHED 17 November 2025

CITATION

de la Cruz-Barrios JD, Abrica-González P, Gutiérrez-Cruz SG, Muñoz-Diosdado A, Mendoza Pérez JA and Sánchez-González AY (2025) Evaluation of the genotoxicity of gold nanoparticles by single-cell electrophoresis. *Front. Nanotechnol.* 7:1673570. doi: 10.3389/fnano.2025.1673570

COPYRIGHT

© 2025 de la Cruz-Barrios, Abrica-González, Gutiérrez-Cruz, Muñoz-Diosdado, Mendoza Pérez and Sánchez-González. This is an openaccess article distributed under the terms of the Creative Commons Attribution License (CC BY).

The use, distribution or reproduction in other forums is permitted, provided the original author(s) and the copyright owner(s) are credited and that the original publication in this journal is cited, in accordance with accepted academic practice. No use, distribution or reproduction is permitted which does not comply with these terms.

Evaluation of the genotoxicity of gold nanoparticles by single-cell electrophoresis

Juan D. de la Cruz-Barrios¹, Paulina Abrica-González^{1,2}*, Sinai G. Gutiérrez-Cruz¹, Alejandro Muñoz-Diosdado¹, Jorge A. Mendoza Pérez³ and Armando Y. Sánchez-González¹

¹Unidad Profesional Interdisciplinaria de Biotecnología del Instituto Politécnico Nacional, Mexico City, Mexico, ²Instituto de Ciencias de la Atmósfera y Cambio Climático de la Universidad Nacional Autónoma deMéxico, Mexico City, Mexico, ³Escuela Nacional de Ciencias Biológicas del Instituto Politécnico Nacional, Mexico City, Mexico

The distinctive characteristics and wide-ranging applications of gold nanoparticles (AuNPs) have sparked considerable scientific interest, leading to increased use and a rise in publications and patents. However, their environmental and genotoxic impact remains poorly understood. In this study, we evaluated the genotoxicity and mutagenicity of AuNPs in germinated roots of *Vicia faba* using three approaches: a comet assay to detect DNA damage, mitotic index analysis, and assessment of chromosomal abnormalities. We observed a reduced mitotic index, increased chromosomal abnormalities, and significant DNA damage in treated samples, indicating genetic alterations and a potential environmental risk. These findings underscore the significance of evaluating the biological effects of AuNPs and demonstrate that single-cell electrophoresis is a reliable tool for assessing genetic damage in plants.

KEYWORDS

AuNPs, comet assay, *Vicia faba*, mutagenicity, mitotic index, chromosomal abnormalities, DNA

1 Introduction

Recently, nanotechnology has become an integral part of various industries, primarily due to the widespread use and development of nanoparticles (NPs), which have driven numerous advances (Malik et al., 2023). While most NPs are engineered, natural NPs also exist, formed in the environment by various physical, chemical, and biological processes.

These include (bio)chemical weathering of minerals, photooxidation, redox and precipitation reactions, and (bio)mineralization processes. Other processes are mechanical fragmentation and gas-solid nucleation in atmospheric systems (Lespes et al., 2020). These processes create many forms of natural nanomaterials in the environment. Such forms include biological structures, like viruses and proteins, and minerals, like clay. Natural colloids include milk and blood (liquid colloids), fog (aerosols), and jelly (gels). Mineralized materials include shells, nacre, bones, insect wings, and opals. Natural fibers, such as spider silk, and functional surfaces, like those of lotus leaves and gecko feet, also contain NPs. Particles from natural events, such as volcanic ash and sea spray, also contain NPs (Lin et al., 2020; Mekuye and Abera, 2023). Most of these NPs can move between Earth's compartments, the biosphere, lithosphere, atmosphere, and hydrosphere (Lespes et al., 2020). In contrast, anthropogenic NPs originate from

industrial processes associated with nanotechnology. These include carbon-based NPs, metallic NPs, dendrimers, and composites (Altammar, 2023; Kumari et al., 2023).

The release of nanomaterials and NPs into the environment can be unintentional or intentional. Unintentional release is often due to human activities. Examples include atmospheric emissions, industrial spills, and wash-off processes that contaminate waterways. Soil can also accumulate NPs from herbicides, electronic waste, and fuel batteries (Alkhaza'leh et al., 2025; Dhanapal et al., 2024; Hernández-Saravia et al., 2023; Martínez et al., 2020). Many airborne particles have been identified in the atmosphere. They come from internal combustion engines, burning of wood and biomass, fossil fuel combustion, natural gas, welding fumes, coal ash, and diesel soot (Donaldson et al., 2005; Portugal et al., 2024). Once dispersed, these NPs can affect air quality, the atmospheric radioactive balance, and hydrometeorological processes.

NPs are also intentionally released through agriculture, with NP-based fertilizers and pesticides developed to enhance crop growth (Mgadi et al., 2024; Tang et al., 2023). Yet, this leads to NPs accumulating in soils and ecosystems, raising long-term environmental concerns. Human-made aerosols, which contain nanoparticles, also influence climate and weather.

These particles scatter and absorb sunlight, which promotes cloud formation. Non-absorbing particles, such as sulfates, cool the climate, while the balance of absorption and scattering determines their net effect (Li et al., 2022; Xiong et al., 2022). Major sources include power plants and vehicles. Climate impact depends on particle growth by vapor condensation; organic NPs are important. Their rapid increase can alter cloud cycles in regions such as the Amazon (Zaveri et al., 2022).

Beyond the air, many NPs accumulate in landfills, where they can leach into the soil and sometimes reach groundwater, posing a risk to water quality and health (Alazaiza et al., 2021; Zahra et al., 2022). In soil, NPs can enter plants. Studies show that NPs smaller than 100 nm from aerosols can enter through leaves, move up stems, and reach the interior tissues (Ha et al., 2021; Yu et al., 2024). Internalization depends on factors such as size, shape, charge, hydrophobicity, chemistry, and stability (Augustine et al., 2020; Sanità et al., 2020).

The cellular uptake of NPOs involves three main mechanisms: endocytosis, phagocytosis, and pore formation in the cell membrane. The last is triggered by mechanical interactions between NPs and the lipid bilayer (Pang et al., 2020; Sousa De Almeida et al., 2021; Toscano and Torres-Arias, 2023). Once inside, NPs can move through plants by apoplastic or symplastic pathways. They cross plasmodesmata and are transported systemically through the xylem vessels (Abrica-González and Gómez-Arroyo, 2022; Djanaguiraman et al., 2024; Sembada and Lenggoro, 2024).

NPs can directly cause DNA damage through ionic dissociation. Indirect effects include membrane disruption, which causes the production of reactive oxygen species (ROS) or changes in antioxidant enzyme activity (Giorgetti, 2019). Their oxidation and breakdown release free radicals, which can inactivate enzymes, cause mutations, and ultimately lead to cell death. This degradation also removes their properties, such as magnetism and fluorescence (Sukhanova et al., 2018).

Metallic NPs harm both eukaryotic and prokaryotic cells by damaging cell walls and membranes, generating ROS and free

radicals, and causing cytotoxicity (Girma, 2023; Gojznikar et al., 2022; Mammari et al., 2022; Sieprawska et al., 2024; Wypij et al., 2021; Zhou et al., 2024). ZnONPs affect corn seed germination and root growth, as well as 40% and 53% of the plumule (Ahmed et al., 2021; López-Moreno et al., 2017). CuNPs are toxic and damage root tissue in *Allium cepa*, lowering mitotic index and raising anomalies, with no normalization during recovery (Velumani et al., 2025).

Genotoxicity refers to the inherent ability of a substance to induce alterations or damage in the genetic material of a cell (Han et al., 2023). Currently, several methods are available to evaluate the genotoxicity of substances, particularly those of NPs. Among the most used methods are the following tests: the micronucleus assay, which detects an extranuclear structure containing unincorporated chromosomal fragments after cytokinesis, surrounded by its membrane and appearing as a small nucleus (Sommer et al., 2020; Vallabani and Karlsson, 2022). Mitotic spindle assembly assay, dividing cells are treated with the substance of interest, and any alterations in the formation of the mitotic spindle are observed (Gomes et al., 2022; Kim et al., 2022; Leem et al., 2022; Santibáñez-Andrade et al., 2022).

The chromosomal aberration test identifies and evaluates structural alterations in chromosomes, such as breaks and rearrangements, which may occur within one chromosome or between chromosomes (Ahluwalia et al., 2023; Hwang, 2024; Landsiedel et al., 2022). The comet assay, also known as single-cell alkaline electrophoresis, is another method. During electrophoresis, DNA fragments unwind and migrate toward the anode, forming a structure resembling a comet tail. The proportion of DNA in the tail indicates the frequency of strand breaks and thus the extent of the damage (Chang et al., 2020; Clementi et al., 2021; Copp et al., 2022; Cordelli et al., 2021; El Yamani et al., 2022; Møller et al., 2020). A relevant example is the use of industrial and consumer products containing gold nanoparticles (AuNPs). Due to their antibacterial properties, they could pose a potential risk to aquatic ecosystems (Adhikari et al., 2025; Mat Lazim et al., 2023).

With the increased commercialization of AuNPs, their release into the environment through manufacturing and waste is inevitable, affecting ecosystems (Teles, 2019). Exposure can occur through water, food, cosmetics, and medications, resulting in various toxicological effects (Sani et al., 2021; Zhang et al., 2024). Only a few studies have evaluated the environmental impact of AuNPs, whereas research on other NPs and their toxicological effects is extensive. However, knowledge in this area remains limited (Kang et al., 2024; Kumah et al., 2023; Rudolf et al., 2024b; 2024a; Wang F. et al., 2024). The use of AuNPs has grown, but their environmental impact, particularly in terms of genotoxicity, remains understudied. To assess the effects on ecosystems, research models are necessary. Plant bioindicators are a promising strategy.

Plants are strong indicators of environmental stress; the types and distribution of certain species show ecosystem health (Cakaj et al., 2024; 2023; Polechońska and Klink, 2023; Roy, 2022; Warnasuriya et al., 2023). Studies have tested genotoxicity in seed sprouts. For example, *Allium Cepa* sprouts exposed to agrochemicals showed chromosome, nucleus, and micronucleus damage (Camilo-Cotrim et al., 2022). Another study investigated the cytotoxic and genotoxic effects of lanthanides (cerium, gadolinium, lutetium) on *Vicia faba* using different media, with

mitotic index and micronucleus frequency as markers (Romero-Freire et al., 2021).

Results showed that lanthanide toxicity depends on the exposure medium, with greater toxicity in the absence of phosphorus, suggesting nutrient availability may influence toxicity in plants (Romero-Freire et al., 2021). Another study assessed the genotoxic, mutagenic, and cytotoxic effects of diclofenac, sulfamethoxazole, and their combination at ambient concentrations in *V. faba*. Parameters analyzed included mitotic index, micronuclei, and chromosomal aberrations. Both drugs, even at ambient concentrations, produced cytotoxic and genotoxic effects in *V. faba*, underscoring the need to monitor pharmaceutical residues in the environment (Drzymała and Kalka, 2024).

In parallel, studies in mammals have also shown that AuNPs can induce size—and concentration—dependent genotoxic effects (Wang et al., 2020) reviewed multiple studies in mammalian cells confirming DNA damage and genome instability caused by AuNPs. Similarly, another study assessed AuNPs of 30, 50, and 90 nm both *in vitro* and *in vivo*, and found that intermediate—sized particles were associated with the most pronounced genotoxic effects (Ávalos et al., 2018). Moreover, another study highlighted that surface characteristics, coating, and dosage represent critical factors determining systemic toxicity in animal models. These references place nanosafety research into a broader context, showing both shared mechanisms and differences between plant and mammalian systems (Niżnik et al., 2024).

The *V. faba* beans is cultivated in over 70 countries, covering approximately 2.2 million hectares and yielding nearly 4 million tons annually (Warsame et al., 2018). This seed is commonly used for genotoxicity, mutagenicity, and cytotoxicity tests (Alavi et al., 2023; Drzymała and Kalka, 2024; Li et al., 2023; Lu et al., 2021; Madnay et al., 2022; Yang et al., 2022; Onisan et al., 2025). The NP market, especially for AuNPs, has expanded. These NPs exist in various environments, but their impact is understudied. In this study, we evaluated their genotoxicity and mutagenicity using the comet assay, mitotic index percentage, and chromosomal aberration analysis. This enabled the assessment of the effects of AuNPs on genetic material.

2 Methodology

2.1 Obtaining AuNPs

The AuNPs used in this study were purchased from Sigma-Aldrich in 5 nm (752,568–25 mL), 20 nm (753,610–25 mL), and 40 nm (753,637–25 mL) sizes. They were stabilized in 0.1 mM PBS at pH 7.0 and stored refrigerated according to the manufacturer's instructions.

2.2 Characterization of AuNPs by TEM

For analysis, 100 μ L of solution was transferred to 3 mL microtube and sealed with Parafilm for transport and storage. To ensure uniform dispersion, the samples were then sonicated for 8 min at 150 W. After sonication, 50 μ L of the suspension was placed on a slide rack and dried under an incandescent lamp for 15 min. Subsequently, the morphological and structural characterization of

the AuNPs was performed using a JOEL JEM-2100 transmission electron microscope at 200 kV (Liu et al., 2021; Patel et al., 2023). Images were acquired in bright-field mode using a high-sensitivity CCD camera, and all characterization procedures were conducted at the Centro de Nanociencias y Micro-Nanotecnologías (CNMN) at the Instituto politécnico Nacional (IPN).

2.3 Characterization AuNPs by UV-Vis

To characterize the AuNPs, 3 mL of solution was extracted using a micropipette. These were split into two 1.5 mL Eppendorf tubes and sealed with Parafilm for safe transport. The tubes were sonicated for 15 min at 150 W. Afterwards, 2.5 mL of the sample was withdrawn and placed in the sample holder. Characterization was performed using a Cintra 2020 spectrophotometer with Cintra version 2.6 software. Measurement specifications: high reading wavelength 700 nm, low 200 nm, reading speed 500 nm/min, step size 0.853 nm, slit width 2.0 nm, and absorbance mode (Biswas, 2021; Dheyab et al., 2020).

2.4 Hydrodynamic diameter, polydispersity index and zeta potential of AuNPs

The hydrodynamic diameter (Z-average), polydispersity (PDI), and zeta potential (ζ-potential) of 5, 20, and 40 nm AuNPs were determined using a Zetasizer Nano ZS (Malvern Panalytical, United Kingdom; He-Ne laser 633 nm, operated with Zeta Sizer software v7.13. The AuNPs, supplied in aqueous suspension of 01 mM PBS, were gently homogenized by inversion prior to analysis. For the surface potential measurements, approximately 1.5 mL of appropriate PNS dilute samples were used (1:20, 1:50, and 1:100). The samples were sonicated for 8 min at 25 $^{\circ}$ C \pm 0.1 $^{\circ}$ C in disposable polystyrene cuvettes (DTS1060). Samples were equilibrated for 120 s at 25 $^{\circ}$ C \pm 0.1 $^{\circ}$ C prior to each run. Three independent runs were performed per replicate. Z-average, PDI, and ζ -potential values were expressed as mean \pm standard deviation. Data quality was considered acceptable for PDI \leq 0.30 and technical variation <10% (Frickenstein et al., 2023; Reipa et al., 2025; Saidi et al., 2024), while ζ -potential values were considered stable when $|\zeta| \ge 25 \text{ mV}$ (Frickenstein et al., 2023; Reipa et al., 2025; Saidi et al., 2024), while ζ-potential values were considered stable when $|\zeta| \ge$ 25 mV (Pourali and Benson, 2025; Wang J. et al., 2024).

2.5 UV-vis characterization of AuNPs as a function of pH

For characterization by pH, 5 mL of AuNP solution was transferred to a 5 mL beaker. The pH was adjusted to 3.0 with hydrochloric acid (HCl). After reaching a pH of 3.0, 2.5 mL was withdrawn and placed in a sample holder. Absorbance was first measured at pH 3.0. The pH was then raised stepwise with NaOH. Absorbance was measured at each pH: 4.0, 5.0, 6.0, 7.0, 8.0, and 9.0. This process was repeated for each step, with the data recorded. pH was measured using a Corning Pinnacle 530 potentiometer (Alam et al., 2022).

2.6 Analysis of the size distribution of AuNPs

The size distribution analysis used TEM images. ImageJ version 1.52u was used for calibration with appropriate scale bars (10 nm for 5 nm AuNPs, 50 nm for 20 nm AuNPs, and 200 nm for 40 nm AuNPs). The diameters of 300 particles per sample were measured manually to ensure representative statistics.

The collected data were exported to OriginLab version 2019b (9.65). The average size, standard deviation, maximum, and minimum values were calculated. Histograms of the particle size distribution were constructed. Curves were fitted to assess uniformity and agreement with nominal values, allowing for a detailed characterization of the size distribution in all samples (Zhang and Wang, 2023).

2.7 Germination of *Vicia faba* (broad bean) seeds

Vicia faba (broad bean) seeds were selected for uniform size, ranging from 2.5 to 2.8 cm. Seeds were placed in water and rubbed to remove impurities. They were surface sterilized in 2.5% sodium hypochlorite for 10 min, then rinsed with sterile water to remove microbial contaminants. After disinfection, the seeds were soaked in clean water for 24 h. This increased their length by 10%–20%, reaching 2.8–3.2 cm.

Seeds were placed on moist cotton and kept in the dark for germination. By the fifth day, the seedlings had developed a primary root of approximately 2.3–2.8 cm. For each experiment, 80 germinating seeds were used, with a germination rate of 90%–95% (Equation 1) (Ali Fayez et al., 2024; Alngiemshy et al., 2020; Neme et al., 2023).

2.8 Preparation of controls

For this study, two control groups and nine experimental treatments were established. The negative control consisted of V. faba roots exposed only to distilled water (T-). In contrast, the positive control was exposed to potassium dichromate ($K_2Cr_2O_7$) at a concentration of 200 μ g/mL (T+), a widely recognized genotoxic agent. Both controls were evaluated in triplicate.

Experimental treatments included AuNPs of three sizes (5, 20, and 40 nm) at three concentrations per size (10, 20, and 30 μ g/mL), for nine total conditions. Each condition was tested in triplicate with a 1-h exposure. After treatment, the roots used for mitotic index and chromosomal abnormality analysis were placed in resting conditions for 24 h of recovery.

2.9 Comet test

To perform this experiment, the slides were thoroughly cleaned. The slides were held up to light to ensure that no visible traces of stains or grease remained. The slides were then sprayed with distilled water to remove any salt residue that may have been present in the tap water. Finally, they were dried in an oven at 37 $^{\circ}\text{C}$ for 20 min. Once the slides were cleaned, they were coverslipped with 40 μL of

standard melting point agarose (NMPA) and allowed to dry. Once covered, they were stored for use on the day of the experiment.

To collect the nuclei, Petri dishes were prepared on ice, and 250 μL of cold phosphate-buffered saline (PBS) was added. A high-carbon steel scalpel blade was used, always kept at a temperature of 3 °C. A broad bean seed was taken, and a 2 cm cut was placed inside a Petri dish containing 250 μL of PBS. After obtaining the broad bean roots were obtained, the end of one of the tips was held with forceps, and seven cuts were made; then, it was placed in the PBS solution. After the nuclei were obtained, the preparations were made on slides that had been previously coated with standard melting point agarose. For this procedure, 10 μL of the cell suspension was combined with 75 μL of low-melting-point agarose (LMPA) inside a 0.5 mL Eppendorf microcentrifuge tube. After combining the nuclei and agarose solution are combined, the mixture is gently blended.

A 75 μ L of the mixture is then applied to a slide that has been previously coated with NMPA. A coverslip is then applied to disperse the nuclei on the surface. After this step, the slide is placed on a cold tray to solidify the LMPA with the nuclei for 5 min. After this time, the coverslip is gently removed, and a new layer of 75 μ L of NMPA is added. A new coverslip is then applied and left on the cold tray for another 5 min to solidify. Finally, the coverslip is removed. The uncovered slides are submerged in a chilled lysis buffer (2.5 M NaCl, 100 mM EDTA, 10 mM Tris pH 10, 1% Triton X-100, 10% DMSO) for a minimum duration of 1 hour. From this point on, work should be conducted in dim light to maintain optimal conditions for the nuclei. Subsequently, the coverslips are removed from the lysis solution, carefully cleaned on the back, and placed in a horizontal electrophoresis chamber containing a buffer at a pH greater than 13 and maintained at cold conditions.

The samples are incubated for 20 min to enable DNA unwinding, after which electrophoresis is carried out under the same time conditions, applying 20 V and 200 mA. An Amersham Pharmacia Biotech electrophoresis chamber, model EPS 601, was used for this procedure. Excess alkaline electrophoresis solution was then removed using neutral buffer (0.4 M Tris), and the sample was immersed in the buffer for 5 min on three occasions. Slides were then fixed with 100% ethanol. Slides were stained with 50 μL of ethidium bromide of 2 $\mu g/mL$ and subsequently observed by fluorescence microscopy.

Analysis was carried out using a ZEISS Axio Scope. A1 optical microscope equipped with a ZEISS Axiocam high-resolution camera. Observations were made at excitation/emission wavelengths of 520-540 nm and 590-620 nm, respectively. The microscope's optical system is infinity-corrected and features interchangeable objectives with magnifications from ×10 to ×100. DNA analysis, including tail length, percentage of DNA in the tail, and tail timing, was performed using Comet Assay IV software, version 4.3. Data on genetic damage parameters were subjected to statistical analysis using GraphPad Prism software (version 10.4.1). Before analysis of variance, an outlier detection test was performed using the Grubbs method to ensure data homogeneity and exclude values that could distort the results. A one-way ANOVA was then applied to assess significant differences between experimental groups.

In cases where statistically significant differences were detected (p < 0.05), Tukey's post hoc test was applied to perform multiple

pairwise comparisons. Data are expressed as mean \pm standard deviation (SD), with a significance threshold set at p < 0.05 (Collins et al., 2023; 2008; Collins et al., 2017; 2002; Darwish et al., 2023; El Yamani et al., 2022; Khalid et al., 2022).

2.10 Calculation of mitotic index and chromosomal aberrations by confocal microscopy

Vicia faba seeds were used, previously washed, disinfected, and germinated according to the protocol described in the previous section. The roots were exposed to AuNPs of three different sizes (5, 20, and 40 nm) at a concentration of 30 μ g/mL. After the exposure period concluded, the roots were gently rinsed with deionized water and placed on a layer of damp cotton for 24 h to facilitate recovery. After this time, approximately 2 cm was cut from the apical region of each root and placed on a concave slide, where they were treated with 5N HCl for 8 min to facilitate cell disaggregation. Subsequently, the acid residues were removed, and two drops of Hoechst 33342 were added at a concentration of 10 mg/mL.

Staining was carried out for 15 min at room temperature in the dark. After the staining time was completed, the samples were carefully washed with distilled water to remove excess fluorochrome. A drop of acetic acid was then added to enhance fixation. The stained root was covered with a coverslip, and gentle pressure (squash) was applied to spread the meristematic cells into a monolayer. The edge of the coverslip was sealed with clear varnish to prevent the sample from drying out during observation. Visualization and analysis were performed using an LSM 710 NLO multiphoton confocal microscope (Carl Zeiss), equipped with a 405 nm excitation laser, which is suitable for detecting the Hoechst 33,342 fluorochrome. Emission was captured between 430 and 480 nm, and ×40 and ×63 infinity-corrected immersion objectives were used.

To ensure statistical representativeness of the analysis, 500 cells were counted for each of the three independent replicates (n = 1,500 cells per experimental condition). The mitotic index was determined by calculating the percentage of cells undergoing division (including prophase, metaphase, anaphase, telophase, and interphase) of the total number of cells counted (Equation 2). Mitotic alterations were classified and identified based on their morphology and frequency. Images were captured digitally with the Zeiss system's integrated camera, and two independent, double-blind observers quantified events. Results were expressed as percentages of cells with alterations relative to the total number of cells analyzed. The data were then statistically analyzed using one-way ANOVA, followed by Tukey's test to determine significant differences between treatments (p < 0.05), as described in Section 3.8 (Klein et al., 2021; Ma et al., 1995; Serrano Ortíz et al., 2024).

3 Results

3.1 Characterization of AuNPs by TEM

TEM images of the 5 nm AuNPs (Figures 1A,B) particularly show predominantly spherical particles with a homogeneous distribution over the support. The uniformity in shape and size is

evident, with few particles outside the expected range. TEM images of the 20 nm AuNPs (Figures 1C,D) reveal mostly spherical particles, with a uniform distribution along the support and minimal evidence of agglomeration. The AuNPs present well-defined edges and, in some cases, internal patterns that could reflect crystalline characteristics. The TEM images of the 40 nm AuNPs (Figures 1E,F) show mostly spherical particles with some slight irregularities in their shape. Some particles exhibit internal contrasts that may be associated with crystalline facets or the material's structural characteristics.

3.2 Characterization of AuNPs by UV-Vis and as a function of pH

The graph shows the absorbance values of 5 nm AuNPs as a function of pH from 3.0 to 9.0 (Figure 2A). In all cases, a maximum absorbance peak (λ max) of 528 nm is observed. At a pH of 7.0, the absorbance peak is higher, indicating optimal stability conditions. On the other hand, at extreme pHs (8.0 and 9.0), the absorbance is slightly lower, which could indicate a reduction in colloidal stability due to possible interactions between the particles. The following graph (Figure 2B) displays the absorbance spectra as a function of pH for 20 nm AuNPs, evaluated within the same range, with a maximum absorbance ($\lambda_{\, \rm max} \!)$ of 535 nm. This is compared to smaller AuNPs, which reflects the increase in size that influences the plasmon resonance. Under neutral conditions (pH), the absorbance is higher, indicating high colloidal stability in this environment. At extreme pH (pH 8.0-9.0), a slight decrease in absorbance is observed. The following graph shows the absorbance spectra of 40 nm AuNPs at different pH values (Figure 2C). A maximum absorbance (λ_{max}) is observed centered at 550 nm, consistent with the increase in size of the NPs. At pH 7, the absorbance is higher compared to basic pH 8.0 and 9.0.

3.3 Hydrodynamic diameter, polydispersity index, CRand zeta potential of AuNPs

The mean hydrodynamic diameter (Z-average) of 5, 20, and 40 nm AuNPs was determined by DLS (Table 1). The measured values were 40.58 \pm 0.35 nm for 5 nm AuNPs, 30.55 \pm 0.17 nm for 20 nm AuNPs, and 55.73 \pm 0.57 nm for 40 nm AuNPs, all consistent with stable scattering profiles and a technical variation below 10%. The polydispersity index (PDI) values obtained were 0.187 \pm 0.010 for 5 nm, 0.197 \pm 0.010 for 20 nm, and 0.106 \pm 0.015 for 40 nm AuNPs. All values were \leq 0.30, indicating monodisperse suspensions and validating the reliability of the hydrodynamic diameter measurements.

The zeta potential (ζ -potential) values were -26.30 ± 2.72 mV (5 nm), -24.20 ± 2.80 mV (20 nm), and -32.63 ± 0.78 mV (40 nm), confirming suitable colloidal stability since values with $|\zeta| \ge 25$ mV are generally considered acceptable. The pH values of the suspensions were 8.32, 7.23, and 7.50 for 5, 20, and 40 nm AuNPs, respectively, remaining within a physiologically stable range. Together, these findings confirm the stable colloidal properties of the AuNPs under the tested conditions (Bhattacharya et al., 2022; Gharibkandi et al., 2023; Maguire et al., 2018).

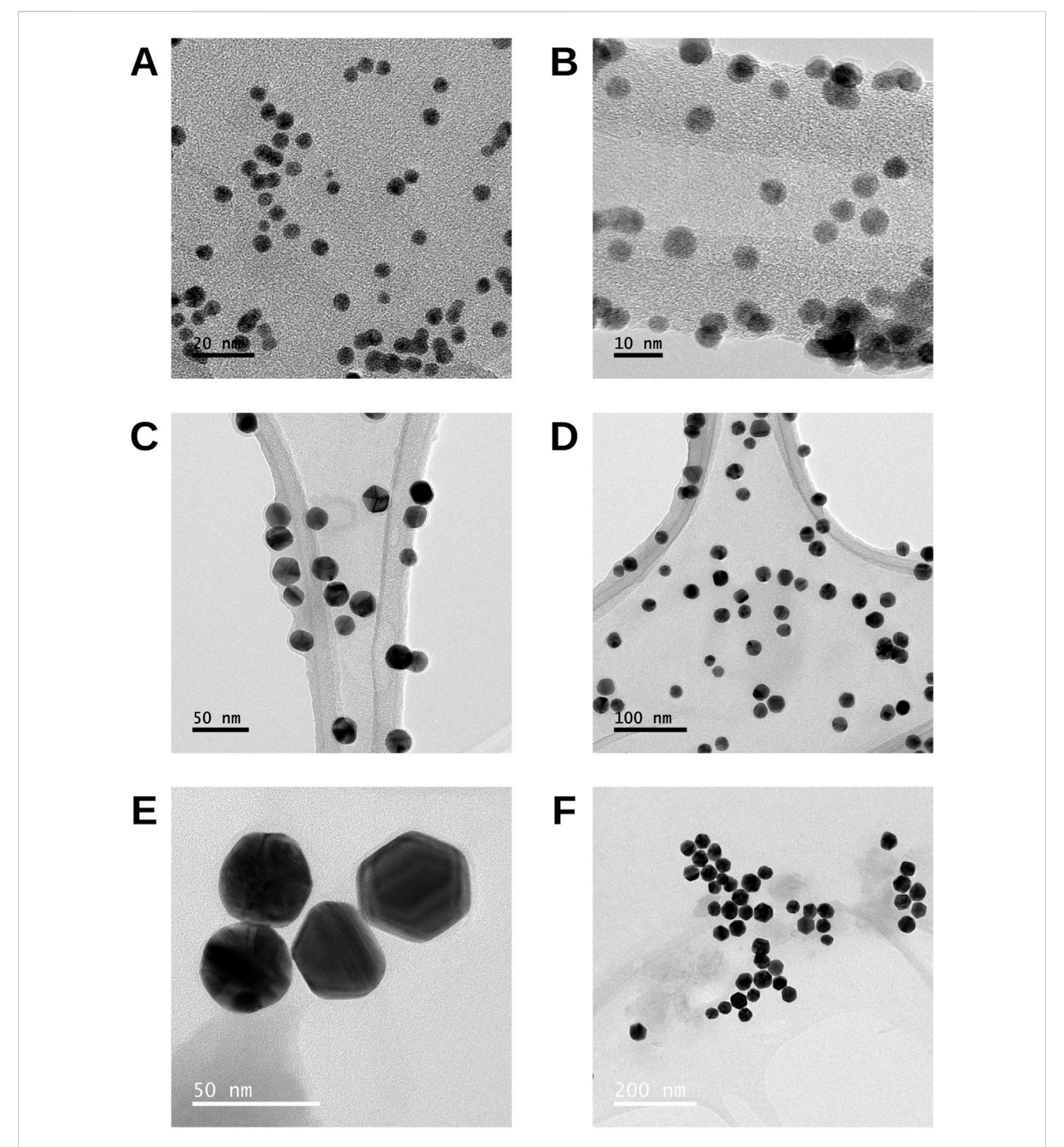


FIGURE 1
TEM images of AuNPs of different sizes. (A,B) 5 nm, (C,D) 20 nm, and (E,F) 40 nm particles. Representative micrographs illustrate the morphology and distribution of the nanoparticles at each nominal size.

3.4 Size distribution analysis of AuNPs

The histogram shows the size distribution of 5 nm AuNPs (Figure 2D). The calculated average size is 5.6 nm, with a standard deviation of ± 0.62 nm, indicating a reasonably uniform distribution around the mean. The observed size distribution spans from 4.11 nm to 6.96 nm.

The following histogram represents the size profile of the 20 nm AuNPs (Figure 2E). Statistical analysis reveals an average diameter of 20.41, with a standard deviation of ± 2.24 , indicating slight variability in diameters. The size range spans from a minimum of 16.08 nm to a maximum of 26.79 nm.

Representing a nominal size of 40 nm, the analysis yields an average size of 40.88 nm with a standard deviation of ± 4.09 ,

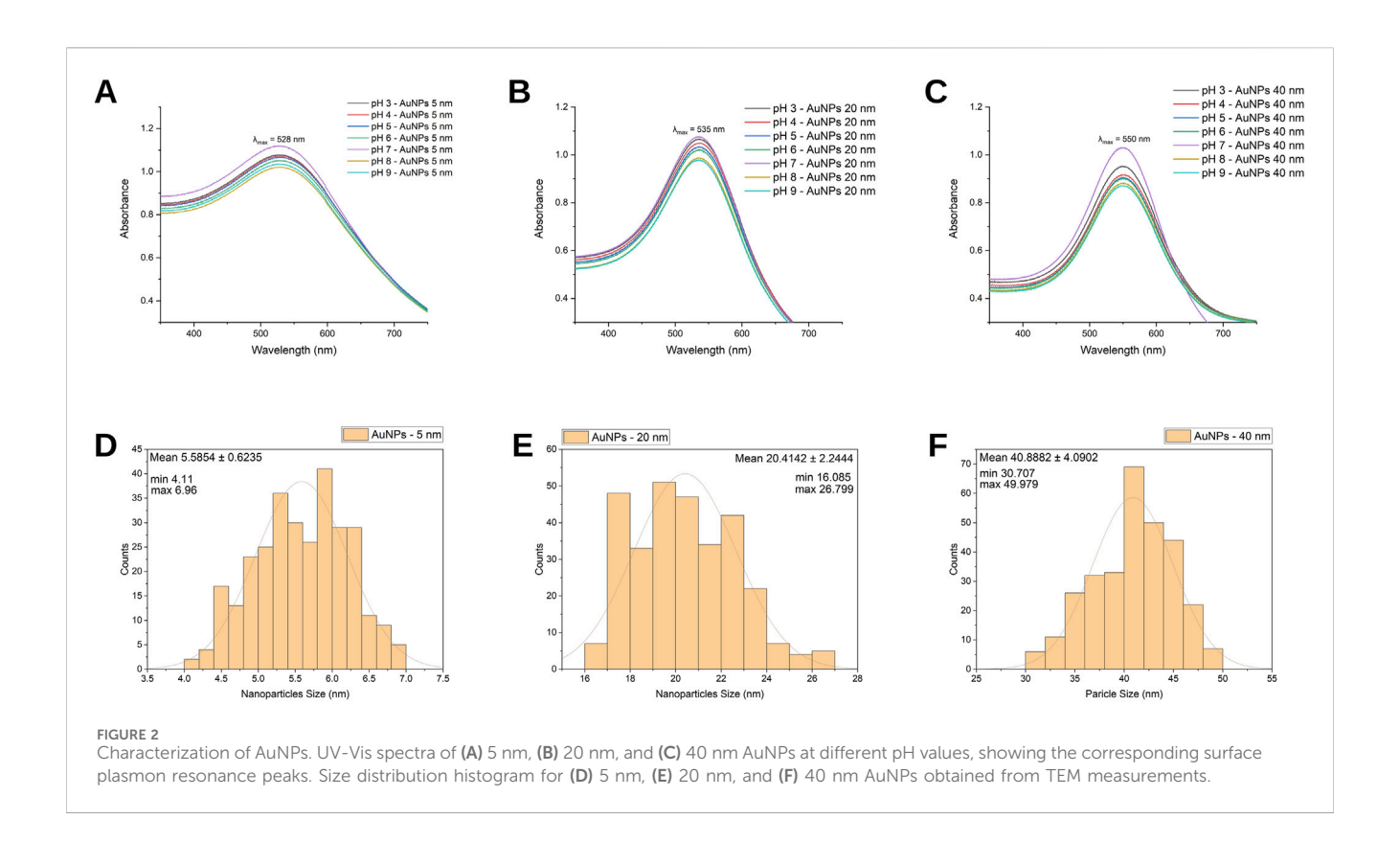


TABLE 1 Hydrodynamic diameter, polydispersity index (PDI), zeta potential, and pH values of AuNPs (5, 20, and 40 nm) measured by DLS and UV-Vis.

Size (nm)	λ (nm)	Hydrodynamic diameter (mean ± SD)	PDI (mean ± SD)	Zeta potential (mean ± SD)	рН
5	499.98	40.58 ± 0.35 nm	0.187 ± 0.010	−26.30 ± 2.72 mV	8.32
20	521.94	30.55 ± 0.17 nm	0.197 ± 0.010	-24.20 ± 2.80 mV	7.23
40	531.00	55.73 ± 0.57 nm	0.106 ± 0.015	−32.63 ± 0.78 mV	7.50

Values are expressed as mean \pm standard deviation (n = 3).

indicating a wider variation compared to smaller sizes. The range goes from a minimum of 30.70 to a maximum of 49.97 (Figure 2F).

3.5 Comet assay

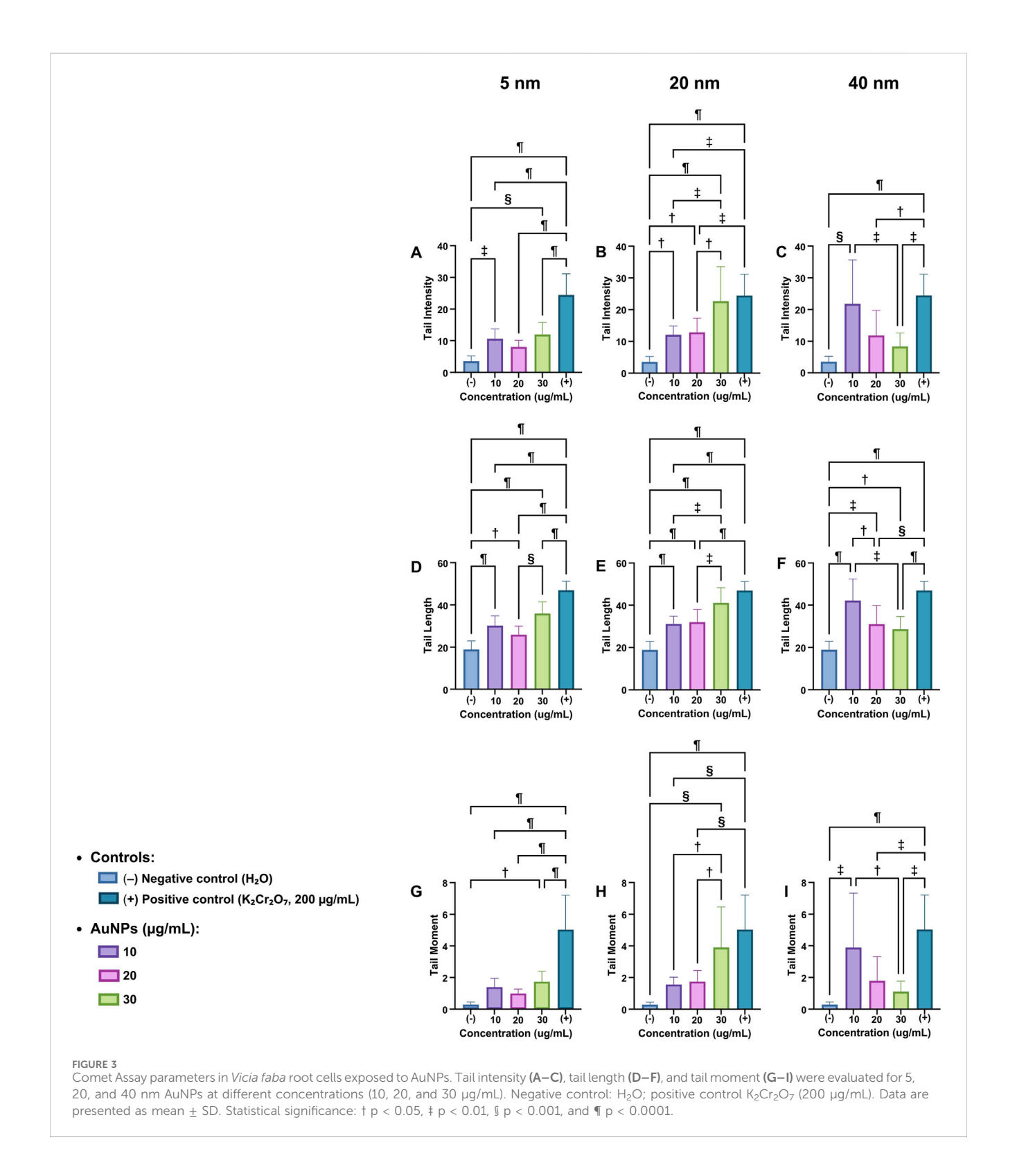
3.5.1 Tail intensity

The Tail Intensity of the comet assay (Figure 3A) shows that 5 nm AuNPs generate DNA damage in a concentration-dependent manner, as assessed by tail intensity. Compared to the negative control (H₂O), AuNPs at 10 μ g/mL increased the tail intensity in a statistically significant manner (‡ p < 0.01), indicating a moderate level of DNA damage.

When exposed to a concentration of 30 μ g/mL, the extent of damage intensified notably, showing a highly significant difference relative to the negative control (§ p < 0.001). At 20 μ g/mL, the damage is considerably lower than at concentrations of 10 and 20 μ g/mL, but still significantly lower than the positive control ($K_2Cr_2O_7$, 200 μ g/mL, ¶ p < 0.0001), which has the highest tailing intensity and serves as a reference for severe DNA damage. For

20 nm AuNPs (Figure 3B), the damage increases in a concentration-dependent manner after treatment. The negative control (H₂O) has the lowest value, while the damage increases significantly at 10, 20, and 30 μ g/mL († p < 0.05, † p < 0.05, and ¶ p < 0.0001) compared to the negative control.

The positive control ($K_2Cr_2O_7$, 200 µg/mL) exhibits the highest damage (¶ p < 0.0001) only with the negative control group, 10 and 20 µg/mL (¶ p < 0.0001, ‡ p < 0.01, and ‡ p < 0.01). In the 40 nm AuNPs (Figure 3C), the negative control (H_2O) presents low values, reflecting a basal level of genotoxic damage. At 10 µg/mL, a significant increase is observed (§ p < 0.001) compared to the negative control, indicating notable genotoxic damage. At a concentration of 20 µg/mL, although damage persists at an elevated level, no statistically significant difference was observed compared to the negative control. At 30 µg/mL, the value decreases slightly compared to 20 µg/mL, but there are no statistically significant differences. The positive control $K_2Cr_2O_7$ shows a significantly higher value than all AuNPs concentrations, being (‡ p < 0.01) with the 30 µg/mL AuNPs, († p < 0.05) with the 20 µg/mL AuNPs, and (¶ p < 0.0001) with the negative control.



3.5.1.1 Tail length

The radar graph shows a concentration-dependent increase with 5 nm AuNPs (Figure 3D). The negative control (H_2O) has the lowest value, while genotoxic damage increases significantly at 10, 20, and 30 µg/mL, and the positive control (\P p < 0.0001, † p < 0.05, \P p < 0.0001 and \P p < 0.0001). Compared to the positive control, there is a statistical difference in all groups, being (\P p < 0.0001) for all groups.

The 20 μ g/mL group showed a statistically significant difference compared to the 30 μ g/mL group (§ p < 0.001).

In Figure 3E, attributed to the 20 nm AuNPs, it is observed that the negative control has the lowest value. Compared to the negative control at 10 μ g/mL, the damage increases significantly (¶ p < 0.0001), and at 20 μ g/mL, the damage is greater, with statistically significant differences of (¶ p < 0.0001). At 30 μ g/mL, it reaches its

highest value among the AuNPs concentrations, being significantly higher and statistically significant (¶ p < 0.0001). Compared to the positive control, a significant difference is found in the groups of 10 and 20 µg/mL AuNPs (¶ p < 0.0001, ¶ p < 0.0001) and the negative control (¶ p < 0.0001). Between the AuNPs groups, there is a significant difference with those of 10 and 20 µg/mL AuNPs compared to the concentration of 30 µg/mL being (‡ p < 0.01 and ‡ p < 0.01).

For the 40 nm AuNPs (Figure 3F), the negative control reflects minimal levels of DNA damage under normal conditions. At 10 µg/mL of AuNPs, the increase is significant compared to the negative control (¶ p < 0.0001). At 20 µg/mL, the damage remains high, with significant differences compared to the negative control (‡ p < 0.01) and a slight decrease compared to 30 µg/mL († p < 0.05), which may reflect variability in the cellular response. The positive control presents the highest value, significantly higher than two concentrations of 40 nm AuNPs of 20 and 30 µg/mL (¶ p < 0.0001). Between groups of AuNPs, there is a significant difference compared to those at 20 and 30 µg/mL, with a concentration of 10 µg/mL being († p < 0.05 and ‡ p < 0.01).

3.5.1.2 Tail moment

For the 5 nm AuNPs (Figure 3G), the negative control (H₂O) exhibits nearly negligible values in contrast to the positive control. No statistically significant differences were observed among the AuNPs-treated groups; significance was found only when compared to the positive control (¶ p < 0.0001). Compared to the positive control, statistically significant differences are found for the three groups of AuNPs at 10, 20, and 30 µg/mL, with p-values of (¶ p < 0.0001) for all three groups. There are no statistically significant differences between the AuNPs groups.

For the 20 nm AuNPs (Figure 3H), genotoxic damage increases in a concentration-dependent manner. The negative control presents practically null values; similarly, there are no statistically significant differences compared to the AuNPs groups. In comparison to the positive control, statistically significant differences were observed in the groups treated with 10 and 20 μ g/mL AuNPs, as well as in the negative control, with significance levels of (§ p < 0.001, § p < 0.001, and § p < 0.0001), respectively. Between groups of AuNPs, statistically significant differences were observed in the concentrations of 10 and 20 μ g/mL compared to the concentration of 30 μ g/mL († p < 0.05).

And for those of 40 nm (Figure 3I), the negative control has the lowest value. At 10 $\mu g/mL$ of AuNPs, a significant increase is observed (‡ p < 0.01) compared to the negative control. At 20 $\mu g/mL$ and 30 $\mu g/mL$, there are no statistically significant differences compared to the negative control. Compared to the positive control, there is a statistically significant difference in the AuNPs groups of 20 and 30 $\mu g/mL$, being (‡ p < 0.01) for both groups. Among the AuNPs groups, the only significant difference was between the 10 and 30 $\mu g/mL$ groups († < 0.05).

Figure 4 shows images obtained from the Comet Assay program during sample analysis, representing the intensity distribution of genotoxic damage in an optical context. In the negative control (H_2O) , the nuclei are compact and lack visible tails, confirming the absence of genotoxic damage.

In the 5 nm AuNP samples, at 10 μ g/mL, genotoxic damage is mild; however, at 20 μ g/mL and especially 30 μ g/mL, the damage

increases significantly, indicating that higher concentrations induce greater DNA fragmentation and migration.

In the 20 nm AuNPs, concentration-dependent genotoxic damage is observed, although to a lesser extent than in the 5 nm samples. At 10 $\mu g/mL$, the damage is mild, while at 20 $\mu g/mL$ it reaches a moderate level, and at 30 $\mu g/mL$, greater genotoxic damage is observed.

At 40 nm, the behavior is different. At 10 μ g/mL, genotoxic damage is moderate, but at higher concentrations (20 and 30 μ g/mL), a decrease in the length and intensity of the tail is observed, indicating less genotoxic damage. On the other hand, the positive control ($K_2Cr_2O_7$, 200 μ g/mL) shows extensive and intense tails in all images, reflecting severe genotoxic damage.

3.6 Mitotic index percentage

3.6.1 Mitotic index percentage by phase

The figure shows the mitotic index (%) for each cell cycle stage—prophase, metaphase, anaphase, telophase, and interphase—in cells treated with AuNPs of 5, 20, and 40 nm at a concentration of 30 μ g/mL (Table 2). Each percentage was calculated using Equation 1 for each phase, based on a total count of 1,500 cells obtained from confocal microscopy images. Representative confocal microscopy images for each cell cycle stage under all treatments are shown in Figure 5.

Images were analyzed with ImageJ software to identify each phase. Data were expressed as percentages using GraphPad Prism. Outliers were identified, and data distribution was assessed using the Shapiro-Wilk normality test. A one-way ANOVA and Tukey's *post hoc* test evaluated group differences.

3.6.1.1 Prophase

The highest value corresponds to the positive control with 53.73%, followed by the 5 nm AuNPs and the negative control with 37%, the 20 nm AuNPs with 36.86%, and finally the 40 nm AuNPs with 33.66%.

3.6.1.2 Metaphase

The highest value is observed in the negative control with 11.20%, followed by 40 nm AuNPs with 11.13%, the positive control with 10.67%, 5 nm AuNPs with 9.67%, and finally, the lowest value of 20 nm AuNPs with 7.27%.

3.6.1.3 Anaphase

40 nm AuNPs have the highest value at 6.40%, followed by the negative control at 5.73%, 20 nm AuNPs at 4.80%, 5 nm AuNPs at 4.67%, and finally, the positive control at 4.46%.

3.6.1.4 Telophase

The highest level is 5 and 40 nm AuNPs with 0.33%, followed by the positive control with 0.13%, 20 nm AuNPs with 0.07%, and the negative control with the lowest value of 0.00%.

3.6.1.5 Interphase

The highest value is observed in 20 nm AuNPs with 51.00%, followed by 40 nm AuNPs with 48.46%, 5 nm AuNPs with 48.33%,

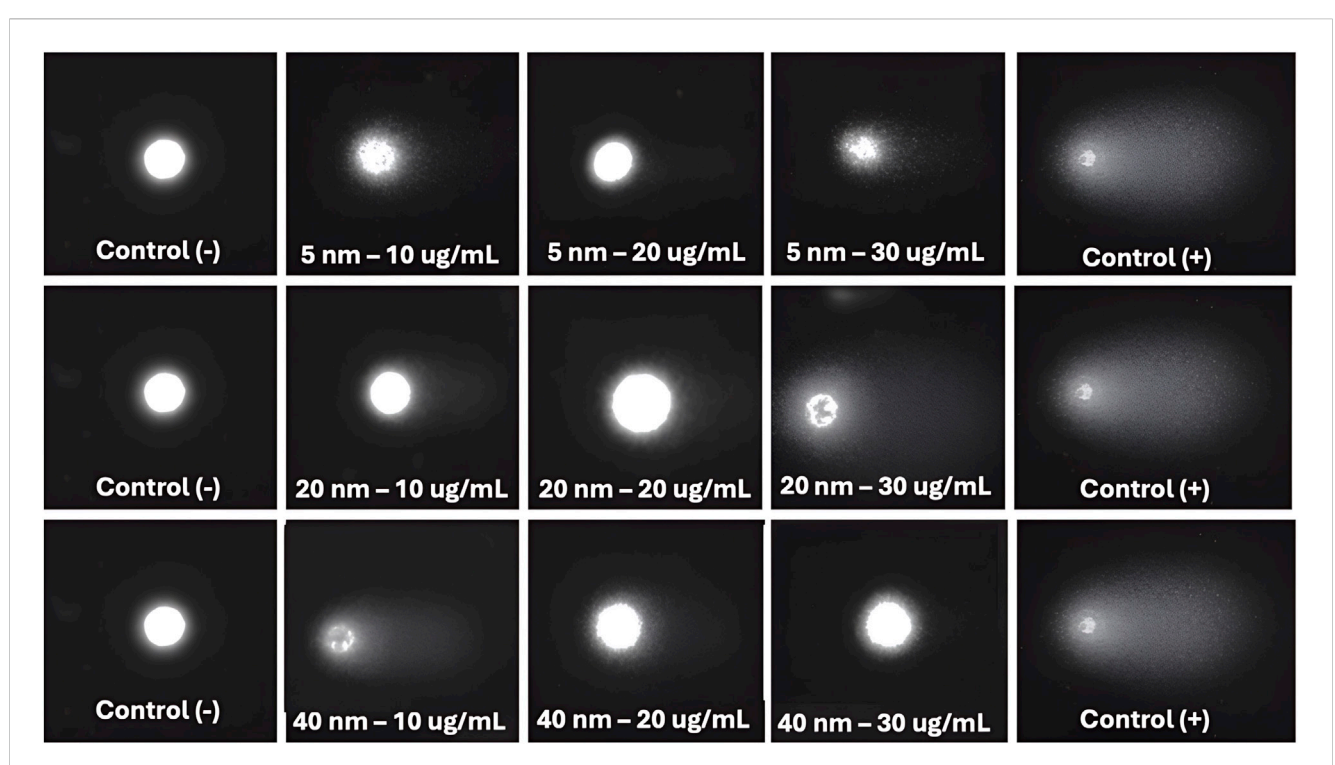


FIGURE 4
Representative images from the Comet Assay program showing the distribution of DNA damage in *Vicia faba* root cells. Negative control Negative control (H_2O) displays intact nuclei without visible tails, while the positive control ($H_2Cr_2O_7$, 200 μ g/mL) exhibits extensive tails. Images correspond to AuNPs of 5, 20, and 40 nm at concentrations of 10, 20, and 30 μ g/mL.

and the negative control with 46.40%. Finally, the lowest value is shown by the positive control with 31.00%

3.6.2 Mitotic index percentage

Experimental measurements determined the percentage of cells in prophase, metaphase, anaphase, and telophase (Figure 6A). These values were combined to calculate the mitotic index (%MI), excluding interphase, as it does not involve cell division. This method produced an accurate measure of mitotic activity in each group.

Outlier testing removed values that could skew the analysis. The Shapiro-Wilk normality test was used to verify the data distribution. If normality was established, a one-way ANOVA was used to compare group means. Tukey's *post hoc* test identified significant differences between specific groups. Statistical analysis revealed substantial differences among groups.

The negative control (H_2O), which represents the basal conditions without treatment, showed a statistically significant difference when compared to each group treated with 5, 20, and 40 nm AuNPs, as well as the positive control ($K_2Cr_2O_7$). The comparison yielded p-values of (‡ p < 0.01) for 5 nm AuNPs, (¶ p < 0.0001) for 20 nm AuNPs, (‡ p < 0.01) for 40 nm AuNPs, and (¶ p < 0.0001) for the positive control. Additionally, the 5 nm AuNPs group differed significantly from the 20 nm AuNPs group († p < 0.05) and the positive control (¶ p < 0.0001). Significant differences were also observed between the 20 nm AuNPs and 40 nm AuNPs groups († p < 0.05), as well as between 20 nm AuNPs and the positive control (p < 0.0001).

The 40 nm AuNPs group also showed a significant difference compared to both the smaller AuNPs (5 and 20 nm) and the positive

control (\P p < 0.0001). These results indicate that AuNPs affect cell division depending on particle size, with 20 nm AuNPs exhibiting a more pronounced inhibitory effect than the other sizes. The response observed with potassium dichromate further validates the experimental design by clearly inducing marked cellular changes. These results underscore the importance of considering nanoparticle size and dosage when assessing their biological effects.

3.6.3 Percentage of chromosomal abnormalities by type

Table 3 displays the percentage of each mitotic abnormality type for all treatments: negative control, 5, 20, and 40 nm AuNPs at 30 μ g/mL, and positive control ($K_2Cr_2O_7$) at 200 μ g/mL.

3.6.3.1 Micronuclei

The positive control showed the highest percentage (15.00%), indicating severe genetic damage and genotoxicity caused by potassium dichromate. The 20 nm AuNPs showed a notable increase (9.53%) compared to the negative control (1.00%), suggesting a greater genotoxic impact due to this specific NP size. The 5 and 40 nm AuNPs also showed increases in micronuclei (5.53% and 8.00% respectively), but lower than the 20 nm ones.

3.6.3.2 Chromosomal bridges

The positive control also showed a significantly higher percentage (4.47%), indicating alterations in chromosome segregation. The 20 nm AuNPs showed the highest values among the NPs (2.73%), followed by the 40 nm (2.20%) and 5 nm (1.80%) ones. In contrast, the negative control is (0.27%).

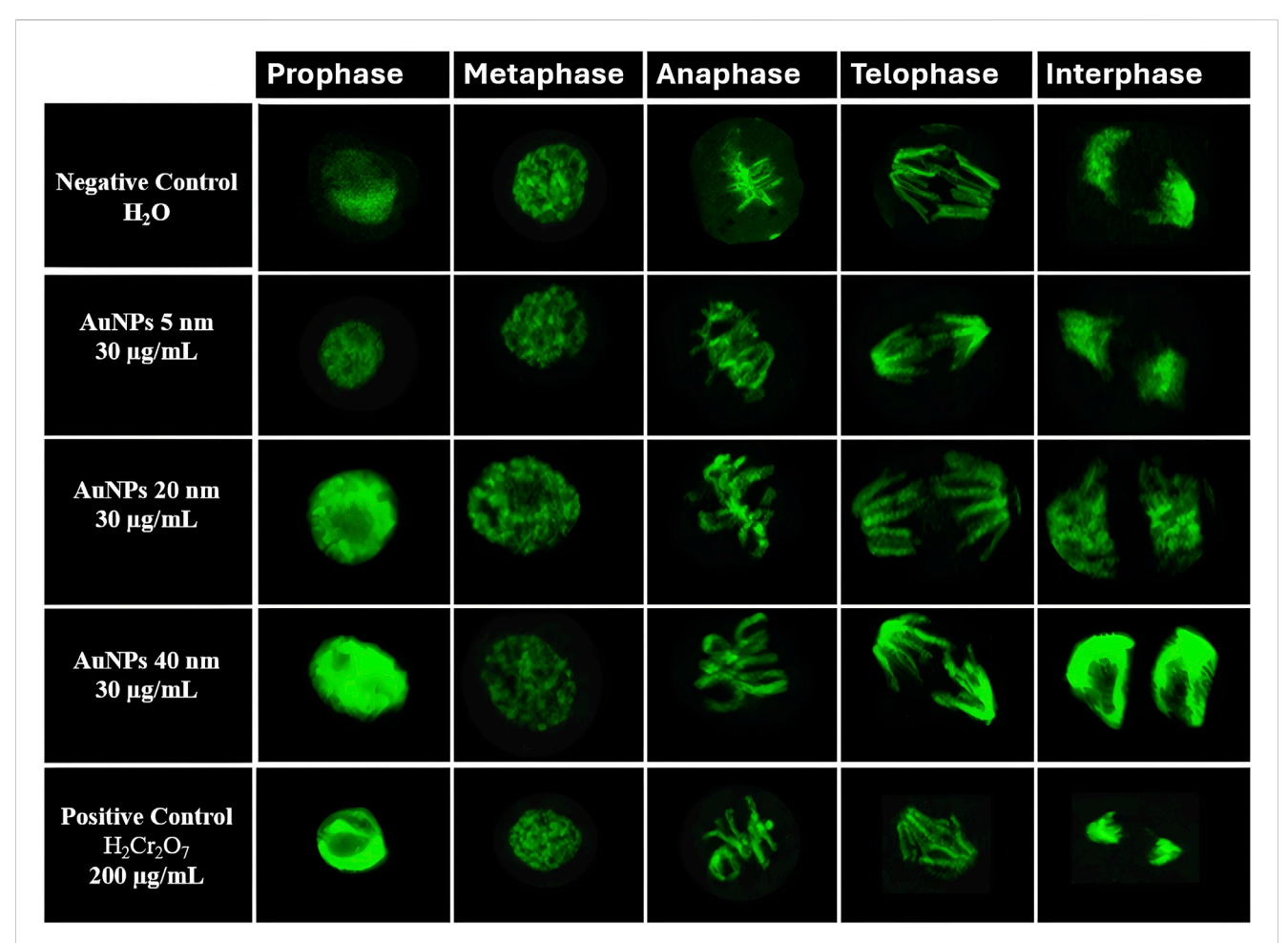


FIGURE 5 Confocal microscopy images of *Vicia faba* root cells at different cell cycle stage (prophase, metaphase, anaphase, telophase, and interphase). Representative images correspond to negative control (H_2O), AuNPs of 5, 20, and 40 nm at 30 μ g/mL, and positive control ($K_2Cr_2O_7$, 200 μ g/mL).

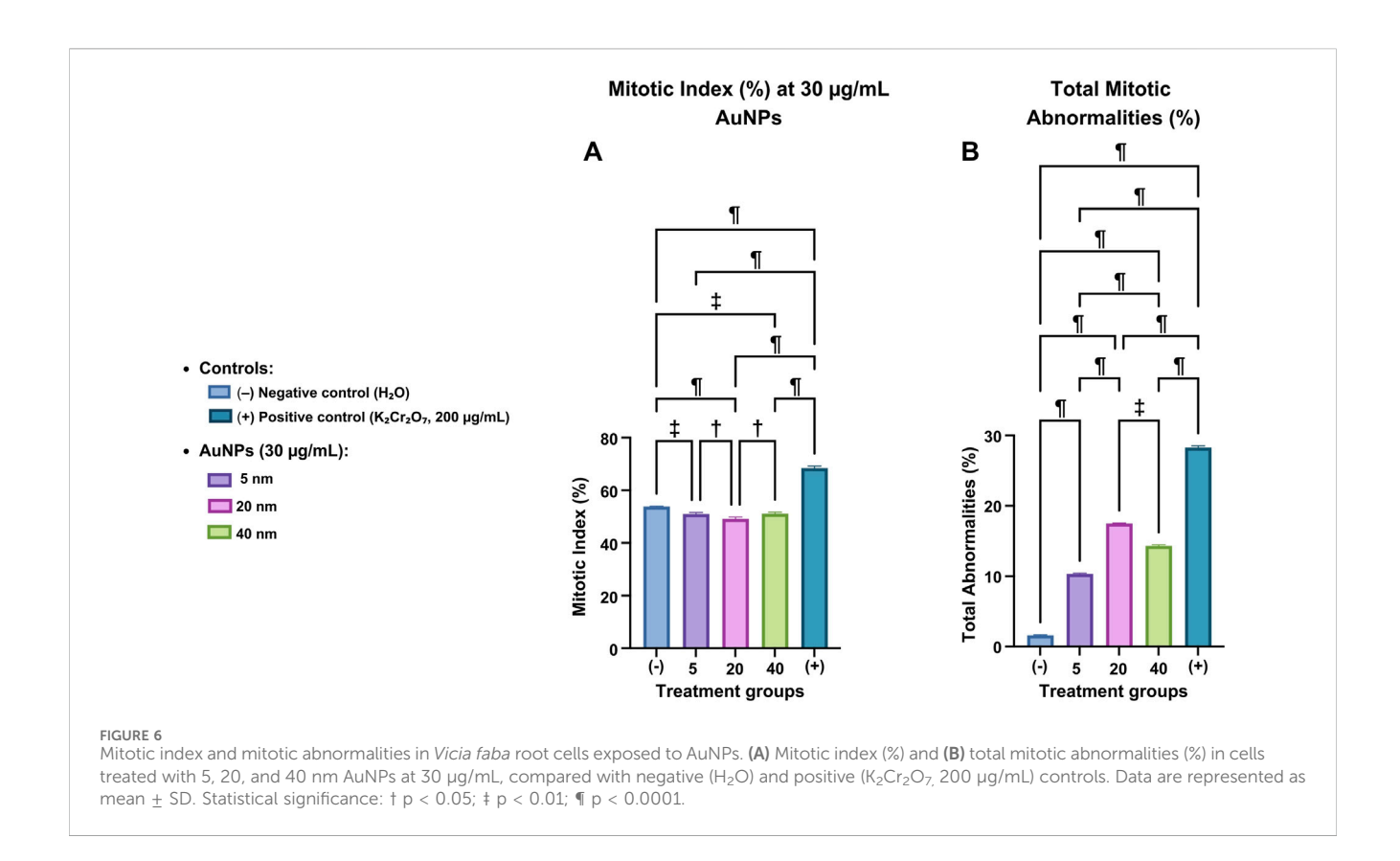
TABLE 2 Distribution of mitotic index phases (% \pm SD) and total mitotic index (TMI % \pm SD).

Species	Groups	Concentrations	Prophase cells (%)	Metaphase cells (%)	Anaphase cells (%)	Telophase cells (%)	Interphase cells (%)	TMI (% ± SD)
Vicia faba	(-) Negative control (H2O)	_	37.00 ± 2.17	11.20 ± 1.40	5.73 ± 1.04	0.00 ± 0.00	46.40 ± 2.24	53.93 ± 2.77
	AuNPs - 5 nm	30 μg/mL	37.00 ± 2.17	9.67 ± 1.34	4.67 ± 0.95	0.33 ± 0.26	48.33 ± 2.24	51.67 ± 2.67
	AuNPs - 20 nm	30 μg/mL	36.86 ± 2.17	7.27 ± 1.16	4.80 ± 0.96	0.07 ± 0.12	51.00 ± 2.24	48.99 ± 2.55
-	AuNPs - 40 nm	30 μg/mL	33.66 ± 2.12	11.13 ± 1.40	6.40 ± 1.10	0.33 ± 0.26	48.46 ± 2.24	51.52 ± 2.71
	(+) Positive control (K ₂ Cr ₂ O ₇)	200 μg/mL	53.73 ± 2.23	10.67 ± 1.38	4.46 ± 0.93	0.13 ± 0.16	31.00 ± 2.08	68.99 ± 2.73

3.6.3.3 Binucleated cells

The positive control stood out with (2.20%), reflecting a higher incidence of cells with errors in cytokinesis. Among the AuNPs,

those of 20 nm showed a higher percentage (1.80%), followed by 5 nm AuNPs and 40 nm AuNPs, for both groups (1.20%). The negative control had the lowest value (0.13%).



3.6.3.4 Multipolarity

The positive control had a higher incidence (2.20%). The 20 nm AuNPs were the highest among the groups (1.20%). The 5- and 40-nm AuNPs had similar values (1.00%). The negative control was the highest value (0.13%).

3.6.3.5 Chromosomal fragmentation

The positive control presented the highest percentage (3.00%), highlighting its impact on genomic stability. The 20 nm AuNPs (1.60%) are the highest group among AuNPs, followed by 40 nm AuNPs (1.40%) and 5 nm AuNPs with a value of 0.60%. The negative control remained low with a value of 0.13%.

3.6.3.6 Anucleated cells

The positive control presented the highest percentage with (1.20%), followed by 20 nm AuNPs with (0.60%), 40 nm AuNPs with (0.47%), and 5 nm AuNPs with (0.27%).

The negative control remained at 0%, serving as the lowest reference group. Results indicate that AuNPs generate mitotic abnormalities depending on size, with 20 nm AuNPs being most genotoxic, followed by 40 nm and 5 nm. The positive control confirms severe damage, validating the experimental model.

3.6.4 Percentage of mitotic abnormalities

Total mitotic abnormalities were quantified as the sum of identified events (micronuclei, chromosome bridges, binucleated cells, multipolarity, chromosome fragmentation, and anucleated cells) out of 1,500 analyzed cells per treatment using confocal microscopy images analyzed with ImageJ (Figure 6B).

Statistical analyses included outlier identification, assessment of normality (Shapiro-Wilk), and a one-way ANOVA followed by Tukey's *post hoc* test to assess group differences.

The negative control showed the lowest basal levels of abnormalities, serving as a reference for normal conditions. 5 nm AuNPs showed a statistically significant increase in abnormalities compared to the negative control (¶ p < 0.0001), indicating a mild genotoxic effect. On the other hand, 20 nm AuNPs exhibited a greater genotoxic effect, with highly significant differences compared to the negative control (¶ p < 0.0001) and the 5 nm AuNPs (¶ p < 0.0001), indicating that they were the most harmful among the treatments evaluated.

The 40 nm AuNPs also showed a significant increase in anomalies compared to the negative control (¶ p < 0.0001) and the 5 nm AuNPs (¶ p < 0.0001). The AuNPs showed to be the treatment that induced the least damage, with significant differences from all groups, as indicated by a value of (¶ p < 0.0001) for all groups. The positive control showed the highest percentage of mitotic abnormalities, with a statistically significant difference from the negative control (¶ p < 0.0001).

3.6.5 Mitotic abnormalities

Figure 7 shows different chromosomal and nuclear alterations under various experimental conditions (negative control, treatment with AuNPs of different sizes, and positive control). Among these alterations are micronuclei, small, spherical bodies composed of chromosomal fragments or entire chromosomes that failed to incorporate into the central nucleus during mitosis, serving as indicators of genetic damage. Their presence is a recognized

TABLE 3 Mitotic abnormalities frequency (%) and total mitotic abnormalities (TMA % + SD) in *Vicia faba* root meristem cells exposed to AuNPs

TMA (% ± SD)	1.65 ± 0.26	10.39 ± 0.54	17.46 ± 0.52	14.27 ± 0.44	28.08 ± 0.62
Anucleated cells	0.00 ± 0.00	0.27 ± 0.10	0.60 ± 0.10	0.47 ± 0.10	1.20 ± 0.23
Chromosomal fragmentation	0.13 ± 0.11	0.60 ± 0.16	1.60 ± 0.25	1.40 ± 0.25	3.00 ± 0.18
Multipolarity	0.13 ± 0.11	1.00 ± 0.18	1.20 ± 0.16	1.00 ± 0.16	2.22 ± 0.27
Binucleated cells	0.13 ± 0.12	1.20 ± 0.18	1.80 ± 0.24	1.20 ± 0.24	2.20 ± 0.18
Chromosomal bridges	0.27 ± 0.13	1.80 ± 0.27	2.73 ± 0.15	2.20 ± 0.15	4.47 ± 0.30
Micronuclei	1.00 ± 0.13	5.53 ± 0.35	9.53 ± 0.31	8.00 ± 0.15	15.00 ± 0.33
Concentrations Micronuclei	I	30 µg/mL	30 µg/mL	30 µg/mL	200 µg/mL
Groups	(-) Negative control (H2O)	AuNPs - 5 nm	AuNPs - 20 nm	AuNPs - 40 nm	(+) Positive control (K ₂ Cr ₂ O ₇)
Species	Vicia faba				

biomarker of genotoxicity, associated with clastogenic or aneugenic effects. According to OECD Guideline 474, their typical morphology includes defined borders, a size less than one-third of the central nucleus, and homogeneous staining.

Chromosomal bridges: Chromosomal bridges are filamentous structures observed during mitosis, serving as anaphase or telophase, which connect opposite poles of a dividing cell. These structures reflect errors in chromosome segregation, such as dicentric fusions, poorly repaired chromosome breaks, or failures in sister chromatid disjunction. Their presence constitutes a cytological marker of genomic instability and genotoxicity. According to OECD Guideline 487 (2020), these abnormalities can be identified by specific nuclear stains, and their analysis is valid for detecting clastogenic activity in plant cells.

Binucleated Cells: Binucleated cells are those that contain two nuclei within the same cytoplasm, resulting from nuclear division without the corresponding cytokinesis. Their presence indicates alterations in the cell cycle, particularly in the final phase of mitosis, and is commonly associated with cytotoxic effects or dysfunctions in the mitotic spindle machinery. These structures are considered a biomarker of interference in normal cell division, as established by OECD Guideline 487 (2020) for genotoxicity studies. In plant cells, their morphology is characterized by nuclei of similar size contained within a single delimited cell.

Multipolarity: Multipolarity is a mitotic alteration characterized by the formation of more than two poles during cell division, which can lead to abnormal chromosome segregation and result in daughter cells with an unequal number of chromosomes, known as aneuploidies. This aberration is typically associated with the disorganization of the mitotic spindle and the malfunction of the microtubule-organizing centers. According to OECD Guideline 487 (2020), multipolarity is a typical manifestation of aneugenic activity and can be identified by optical or confocal microscopy in cells in metaphase or anaphase.

Chromosomal fragments: Chromosomal fragments are small structures, not linked to the mitotic spindle, that result from breaks in chromosomes due to severe clastogenic damage. These fragments lack a centromere, so they are not adequately distributed during mitosis, remaining free in the cytoplasm or giving rise to micronuclei. Their presence reflects a severe disorganization of the genetic material and is a direct indicator of genotoxicity. According to OECD Guideline 487 (2020), their observation in plant cells is valid for identifying clastogenic agents. Morphologically, they are identified as small bodies, separated from the central nucleus, homogeneous staining.

Anucleated cells: Anucleated cells are those that have entirely lost their nucleus, indicating an extreme level of cellular damage or progression to cell death. In the context of genotoxicity studies, their presence serves as a morphological indicator of severe cytotoxicity, possibly induced by exposure to chemical agents that disrupt nuclear integrity or cause advanced apoptosis. According to OECD guidelines (TG 487, 2020), these cells should be considered when assessing cytotoxic effects along with other nuclear abnormalities (Animasaun et al., 2024; DiPeso et al., 2025; OECD, 2016; Liman et al., 2025; Owolarafe et al., 2020; Sarsar et al., 2025; Üstündağ et al., 2023; Zarnescu et al., 2024).

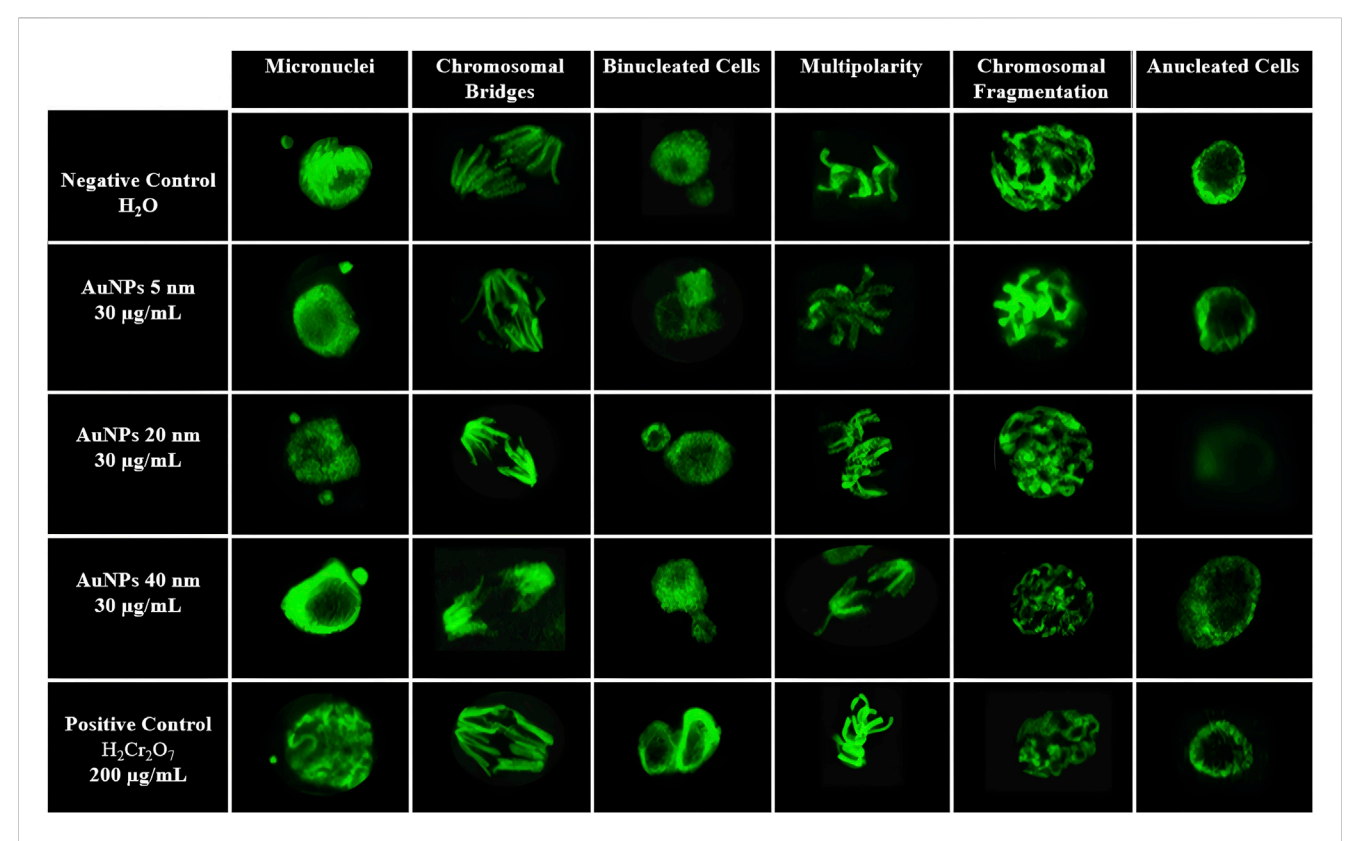


FIGURE 7
Representative confocal microscopy images of mitotic abnormalities in *Vicia faba* root cells. Show are micronuclei, chromosomal bridges, binucleated cells, multipolarity, chromosomal fragmentation, and anucleated cells in samples treated with AuNPs of 5, 20, and 40 nm (30 μ g/mL), compared with negative (H_2O) and positive ($K_2Cr_2O_7$, 200 μ g/mL) controls.

4 Discussion

The morphology and even distribution of AuNPs seen in the TEM images suggest a controlled and reproducible synthesis (Jiménez-Martínez et al., 2024; Song et al., 2011). Internal patterns and contrasts in 20- and 40-nm AuNPs may result from the formation of specific crystalline facets during particle growth (Liu et al., 2007). AuNP characteristics match the supplier's specifications. In UV-Vis characterization, the absorbance of AuNPs at extreme pH values (8 and 9) decreases slightly, potentially indicating reduced colloidal stability due to particle interactions (Pourali et al., 2021). Larger AuNPs show greater absorbance, likely due to size effects on plasmon resonance that shift the SPR peaks to higher wavelengths (Annur et al., 2018; Ershov et al., 2016). Absorption between 500 and 550 nm confirms these are gold nanoparticles (Oliveira et al., 2023; Santhoshkumar et al., 2017). The presented histograms show average sizes of 5.5854, 20.4142, and 40.8882 nm. Notably, size variability increases with the size of AuNPs (Melo et al., 2021). Smaller particles display uniform size distributions, while larger ones have more dispersed diameters, in line with other reports (Xia et al., 2019).

The hydrodynamic diameter obtained by DLS were consistently larger than those observed by TEM, particularly for the smallest nanoparticles. This discrepancy is well documented and arises from the contribution of the solvation shell and the electrical double layer, which account for a greater fraction of the apparent size in ultrasmall particles. Therefore, DLS does not contradict TEM structural

findings but rather complements them by capturing particle—medium interactions. The polydispersity index (PDI) values remained below 0.30 across all AuNPs sizes, confirming monodispersity and validating the reliability of the hydrodynamic diameter measurements. This narrow size distribution supports the reproducibility and stability of the nanoparticles suspensions, an essential criterion for biological and environmental applications.

Regarding colloidal stability, the negative zeta potentials obtained are consistent with citrate-stabilized AuNPs under similar conditions, as reported in recent studies. Although intermediate-sized particles exhibited slightly lower magnitudes, the values remained within the acceptable threshold for stability ($|\zeta| \geq 20$ mV). These findings confirm that the suspensions retained sufficient electrostatic repulsion to prevent aggregation. Taken together—considering UV-Vis spectra, size distribution by TEM, DLS-derived hydrodynamic diameters and PDIs, and ζ -potential values—the AuNPs demonstrate physicochemical robustness. These results align with recent reports on AuNPs with biomedical potential, supporting their reliability as experimental nanomaterials (Fathy et al., 2023; Filippov et al., 2023; Kuznetsova et al., 2022).

The results of the comet assay (Tail Intensity) demonstrate that AuNPs induce genotoxic damage in a manner dependent on both size and concentration. This effect is consistent with the higher specific surface area an increased cellular interaction of smaller particles, which facilitates stronger biological activity (Li et al., 2010; Pan et al., 2007). In the case of 20 nm AuNPs, significant

genotoxicity was also detected, though to a lesser extent than with 5 nm AuNPs, particularly at higher concentrations. This indicates a reduced reactivity compared to smaller particles, a trend supported by the literature, which reports decreasing DNA damage as particle size increases (Mironava et al., 2010; Woźniak et al., 2017). Finally, 40 nm AuNPs displayed nonlinear behavior, with the greatest DNA damage observed at 10 µg/mL but lower effects at higher concentrations, which may be related to reduced cellular interaction under these conditions—a phenomenon previously described in other studies (Barillet et al., 2010; Shukla et al., 2011).

Tail Moment results confirm that AuNPs cause genotoxic damage in a size- and concentration—dependent manner. Exposure to 5 nm AuNPs produced a significant increase in Tail Moment with rising concentrations, which reflects the strong biological activity associated with their high surface-to-volumen ratio and capacity for cellular interaction (Hu et al., 2022; Lebedová et al., 2018). Similarly, 20 nm AuNPs caused a significant rise in the Tail Moment at medium and high concentrations, indicating a moderate genotoxic potential, as reflected in studies on intermediate-sized NPs affecting plant root cells and mitosis (Debnath et al., 2018; Siddiqi and Husen, 2017). For 40 nm AuNPs, the most significant DNA damage was observed at low concentrations, with decreasing effects at higher doses, a nonlinear trend that may be related to changes in particles behavior under these conditions—a pattern also described in other studies (Štefanić et al., 2021).

In the percentage of mitotic index, the positive control presented the highest rate, probably due to a compensatory proliferative response to the genotoxic damage induced by potassium dichromate. This phenomenon has been documented in studies on genotoxic stress in plant cells (Patlolla et al., 2009; Mitra and Chattopadhyay, 2013; Uyeki et al., 1983). The negative control showed a basal percentage, reflecting normal growth conditions without extreme stress (Kato and Haskins, 2023; Lotze et al., 2004). Treatment with 5 nm AuNPs resulted in a moderate reduction in the mitotic index relative to the negative control. Their small size facilitates interaction with meristematic cells, which can interfere with cycle progression and reduce cell division frequency (Li et al., 2010; Pan et al., 2009; Ramalingam et al., 2016). In contrast, 40 nm AuNPs caused a more significant reduction in the mitotic index. Their larger size favors agglomeration, which limits cellular uptake but can still disrupt mitotic organization, leading to altered division patterns (Li et al., 2018a; Pan et al., 2007; Rajeshwari et al., 2016). The most pronounced effect was observed with 20 nm AuNPs, which produced the lowest mitotic index. This size appears to be particularly effective at interfering with cellular components, disrupting mitotic dynamics and causing cell cycle arrest (Debnath et al., 2018; Li et al., 2018b; Nirmala and Lopus, 2019).

The results from chromosomal aberrations demonstrate that the genotoxic effect is size—dependent, with 20 nm AuNPs inducing the highest percentage of aberrations, followed by 40 nm and 5 nm AuNPs, respectively. This behavior suggests that 20 nm AuNPs represent an optimal size for cellular internalization and interaction with components of the mitotic apparatus and genetic material, which enhances the likelihood of chromosomal alterations (Tsai et al., 2022; Vales et al., 2020). In contrast, smaller AuNPs (5 nm) may be more prone to aggregation or elimination, while larger ones (40 nm) mayhave a reduced ability to penetrate cells, resulting in

comparatively lower levels of aberrations (Carnerero et al., 2020; Fu et al., 2021; Xia et al., 2019).

Taken together, the results demonstrate that AuNPs induce significant alterations in the mitotic apparatus and compromise the stability of genetic material in the meristematic cells of *V. faba*. These effects are clearly size—dependent. The chromosomal abnormalities identified—including chromatid bridges, fragments, micronuclei, and binucleated cells—represent direct consequences of AuNPs interaction with critical components of the cell cycle, particularly during mitotic progression.

AuNPs internalized by plant cells may localize in the cytoplasm and, depending on their size and active surface, can cross the nuclear envelope. Once inside, they can interact directly with proteins that are essential for cell function. For instance, they alter α/β tubulins, which are required for microtubule polymerization. They can also interfere with cell cycle regulators, such as cyclins and cyclindependent kinases (CDKs), as well as proteins responsible for the spindle assembly checkpoint. These disruptions ultimately result in errors in mitotic spindle assembly, improper kinetochore capture, and failures in the segregation of chromosomes or chromatids. These cellular disruptions result in distinct structural changes. Chromosome bridges may form from poorly repaired breaks or dicentric fusions. Chromosome fragments can result from unsegregated acentric breaks. Micronuclei arise when some genetic material is left out of the main nucleus after telophase. The presence of binucleated cells suggests direct interference with cytokinesis, possibly due to damage to contractile ring proteins or problems with late mitotic signals.

In terms of size, 20 nm AuNPs produced the most significant mitotic disruption. This effect is attributed to the optimal size for cellular internalization, which provides greater contact with structures, such as centrosomes, sensitive intracellular chromosomes, and microtubules. Their high surface-to-volume ratio further enhances the likelihood of interactions with protein residues and DNA nucleobases, potentially leading to structural alterations such as alkylation or cross-linking that compromise genomic integrity. Collectively, these results demonstrate that AuNPs act as physical entities capable of initiating molecular responses that effect cell cycle regulation, chromosome stability, and overall cell viability. Their size-dependent genotoxic and cytotoxic effects underscore the importance of considering physicochemical parameters when designing and applying AuNPs in agricultural, biomedical, and environmental contexts, particularly when targeting highly proliferative organisms (Kato and Haskins, 2023; Warr et al., 1993; Yoon et al., 2025).

Overall, the results obtained in *V. faba* are consistent with those reported in mammalian models, where smaller AuNPs exhibit grater genotoxicity due to their higher specific surface area (Mironava et al., 2010; Vales et al., 2020). However, notable differences are observed: in some plants, larger particles still induce chromosomal abnormalities attributable to mitotic alterations, whereas in animal cells their effect tends to be lower due to limited internalization, depending on the size, surface, and functionalization of AuNPs (De Berardis et al., 2020; Niżnik et al., 2024; Xia et al., 2017).

These contrasts reflect that, although there is common size- and concentration-dependent pattern across biological systems, the magnitude and mechanisms of damage depend on the experimental model used. Our study provides evidence in higher

plants that complements what has been observed in animal cells, reinforcing the idea that nanosafety evaluation of AuNPs should consider both plant and animal organisms.

5 Conclusion

This study evaluated the effects of AuNPs of different sizes (5, 20, and 40 nm) on the meristematic cells of *V. faba* roots. For mitotic index and chromosomal aberration analysis, only the 30 µg/mL concentration was used, as it showed significant and differentiated variation in the comet assay (Tail Intensity, Tail Length, Tail Moment). This allowed for a targeted analysis of effects after acute exposure (1 h) and a 24-h recovery period. Among comet parameters, the Tail Moment was chosen as the primary indicator of genotoxic damage, providing a comprehensive view of DNA breakage by combining tail length and intensity, rather than using each parameter separately.

Tail Moment results across the three sizes at a concentration of 30 revealed an order of increasing damage: positive control >20 nm AuNPs >5 nm > 40 nm > negative control. This indicates that 20 nm AuNPs are the most efficient in generating DNA breaks, likely due to their optimal size for cell penetration and interaction with nuclear structures. Accordingly, the total mitotic signature, assessed after 24 h of recovery, showed a significant decrease in cells treated with AuNPs in the order: positive control > negative control >5 nm AuNPs >40 nm > 20 nm. This pattern reflects a cell cycle arrest in response to genetic damage. The reduction in the mitotic index suggests that cells activate checkpoint mechanisms to prevent the proliferation of cells with compromised DNA integrity. Analysis of the total percentage of chromosomal aberrations reinforced these findings, with the following pattern observed: positive control >20 nm AuNPs >40 nm AuNPs >5 nm > negative control.

The 20 nm AuNPs caused the highest number of structural alterations during mitosis, suggesting a direct interference with the mitotic spindle and chromosome condensation. This contributes to greater genetic instability. Together, the integrated results of the three parameters indicate a direct correlation between DNA damage, mitotic disruption, and chromosomal abnormalities, most pronounced with 20 nm AuNPs. The 5 nm particles exhibited an intermediate effect, possibly limited by aggregation or elimination, but still caused genetic damage. In contrast, 40 nm particles exhibited a lower penetration capacity.

These results underscore the importance of AuNP size in assessing biological safety and confirm the sensitivity of the V. faba assay to study nanomaterial genotoxicity for applications in agriculture and biomedicine.

6 Equations

GP (%) =
$$\frac{\text{number of germinated seeds}}{\text{total seeds sown}} \times 100$$
 (1)

Equation 1: Germination Percentage

$$MI = \frac{\text{Number of cells in mitosis}}{\text{Total number of cells}} \times 100$$
 (2)

Equation 2: Mitotic Index

Data availability statement

All data generated for this study are included in the article. Further inquiries can be directed to the corresponding author.

Author contributions

JD-CB: Writing - original draft, Investigation, Software, Formal Analysis, Writing - review and editing, Project administration, Methodology. PA-G: Conceptualization, Validation, Methodology, Supervision, Investigation, Funding acquisition, Writing - review and editing, Formal Analysis, Resources, Writing - original draft. SG: Project administration, Investigation, Writing - review and editing, Methodology, Formal Analysis. AM-D: Funding acquisition, Resources, Visualization, Validation, Formal Analysis, Supervision, Investigation, Writing - review and editing. JM: Conceptualization, Methodology, Writing - review and editing, Supervision, Validation, Formal Analysis, Visualization. AYS-G: Methodology, Investigation, Project administration, Writing - review and editing.

Funding

The author(s) declare that financial support was received for the research and/or publication of this article. The research was funded by CONAHCYT (Consejo Nacional de Humanidades, Ciencias y Tecnologías) México under grant number 4647203. JD-CB is a researcher under the Secretaría de Ciencia, Humanidades, Tecnología e Innovación program (Sistema Nacional de Centros Públicos de Invesgación Científica y Tecnológica), supported by CONAHCYT.

Acknowledgements

The authors wish to thank the Secretaría de Investigación y Posgrado and the Centro de Nanociencias y Micro-Nanotecnologías (CNMN) of the Instituto Politécnico Nacional (IPN), the Instituto Nacional de Ciencias de la Atmósfera y Cambio Clímatico (ICAyCC) of the Universidad Nacional Autónoma de México (UNAM), and the CONAHCYT (Consejo Nacional de Humanidades, Ciencias y Tecnologías), now known as Secretaría de Ciencia, Humanidades, Tecnología e Innovación (Sistema Nacional de Centros Públicos de Investigación y Cátedras de Investigación Científica y Tecnológica).

Conflict of interest

The authors declare that the research was conducted in the absence of any commercial or financial relationships that could be construed as a potential conflict of interest.

Generative Al statement

The author(s) declare that no Generative AI was used in the creation of this manuscript.

Any alternative text (alt text) provided alongside figures in this article has been generated by Frontiers with the support of artificial intelligence and reasonable efforts have been made to ensure accuracy, including review by the authors wherever possible. If you identify any issues, please contact us.

References

Abrica-González, P., and Gómez-Arroyo, S. (2022). Effects and characterization of atmospheric nanoparticles (CuO, ZnO NPs) in plants. *Rev. Int. Contam. Ambient.* 38, 145–164. doi:10.20937/rica.54303

Adhikari, L., Todorov, T. I., Yang, T., Hornick, J., Sawant, R., Paulose, T., et al. (2025). Silver migrates to solid foods and abiotic surfaces from model plastic packaging containing silver nanoparticles. ACS Food Sci. Technol. 5, 659–669. doi:10.1021/acsfoodscitech.4c00813

Ahluwalia, K. K., Thakur, K., Ahluwalia, A. S., Hashem, A., Avila-Quezada, G. D., Abd_Allah, E. F., et al. (2023). Assessment of genotoxicity of zinc oxide nanoparticles using mosquito as test model. *Toxics* 11, 887. doi:10.3390/toxics11110887

Ahmed, B., Rizvi, A., Syed, A., Elgorban, A. M., Khan, M. S., Al-Shwaiman, H. A., et al. (2021). Differential responses of maize (Zea mays) at the physiological, biomolecular, and nutrient levels when cultivated in the presence of nano or bulk ZnO or CuO or Zn²⁺ or Cu²⁺ ions. *J. Hazard Mater.* 419, 126493. doi:10.1016/j.jhazmat.2021.126493

Alam, M. S., Farhad, S. F. U., Tanvir, N. I., Bitu, M. N. A., Moniruzzaman, M., Hakim, M., et al. (2022). Spherical and rod-shaped gold nanoparticles for surface enhanced Raman spectroscopy. 2022 4th International Conference on Sustainable Technologies for Industry 4.0 (STI 2022), Dhaka, Bangladesh, December 17–18, 2022. doi:10.1109/ati56238.2022.10103260

Alavi, E., Tajadod, G., Jafari Marandi, S., and Arbabian, S. (2023). *Vicia faba* seed: a bioindicator of phytotoxicity, genotoxicity, and cytotoxicity of light crude oil. *Environ. Sci. Pollut. Res.* 30, 21043–21051. doi:10.1007/s11356-022-23244-w

Alazaiza, M. Y. D., Albahnasawi, A., Ali, G. A. M., Bashir, M. J. K., Copty, N. K., Amr, S. S. A., et al. (2021). Recent advances of nanoremediation technologies for soil and groundwater remediation: a review. *Water* 13, 2186. doi:10.3390/w13162186

Ali Fayez, K., El-Deen Mohamed Radwan, D., Ahmed Faheed, F., and Edrees El-Sayed, A. (2024). Gibberellic acid improves seed germination and growth of *Vicia faba* plants subjected to clethodim herbicide. *Sohag J. Sci.* 2025, 24–33. doi:10.21608/sjsci. 2024.306751.1216

Alkhaza'leh, H., Rahbeh, M., Hamadneh, I., Al-Mashakbeh, H., and Albalawna, Z. (2025). Nanoparticles in soil reclamation: a review of their role in reducing soil compaction [ahead of print]. doi:10.1177/11786221241311725

Alngiemshy, N. F., Alkharafi, J. S., Alngiemshy, N. F., Alkharafi, J. S., Alharbi, N. S., and Al-Sowayan, N. S. (2020). Effect of seeds size on germination of faba bean plant. *Agric. Sci.* 11, 457–463. doi:10.4236/as.2020.115028

Altammar, K. A. (2023). A review on nanoparticles: characteristics, synthesis, applications, and challenges. *Front. Microbiol.* 14, 1155622. doi:10.3389/fmicb.2023. 1155622

Animasaun, D. A., Adedibu, P. A., Afolabi, S. O., Abdulkareem, K. A., Ibrahim, S., and Krishnamurthy, R. (2024). Hazard assessment and cytogenotoxic effect of different concentrations of mercury chloride sterilant using the *Allium cepa* assay. *Discov. Toxicol.* 1 (1 1), 2–10. doi:10.1007/s44339-024-00002-w

Annur, S., Santosa, S. J., and Aprilita, N. H. (2018). PH dependence of size control in gold nanoparticles synthesized at room temperature. *Orient. J. Chem.* 34, 2305–2312. doi:10.13005/ojc/340510

Augustine, R., Hasan, A., Primavera, R., Wilson, R. J., Thakor, A. S., and Kevadiya, B. D. (2020). Cellular uptake and retention of nanoparticles: insights on particle properties and interaction with cellular components. *Mater Today Commun.* 25, 101692. doi:10. 1016/j.mtcomm.2020.101692

Ávalos, A., Haza, A. I., Mateo, D., and Morales, P. (2018). *In vitro* and *in vivo* genotoxicity assessment of gold nanoparticles of different sizes by comet and SMART assays. *Food Chem. Toxicol.* 120, 81–88. doi:10.1016/J.FCT.2018.06.061

Barillet, S., Simon-Deckers, A., Herlin-Boime, N., Mayne-L'Hermite, M., Reynaud, C., Cassio, D., et al. (2010). Toxicological consequences of TiO₂, SiC nanoparticles and multi-walled carbon nanotubes exposure in several mammalian cell types: an *in vitro* study. *J. Nanoparticle Res.* 12, 61–73. doi:10.1007/s11051-009-9694-y

Bhattacharya, S. R., Bhattacharya, K., Xavier, V. J., Ziarati, A., Picard, D., and Bürgi, T. (2022). The atomically precise Gold/Captopril nanocluster Au25(Capt)18 gains

Publisher's note

All claims expressed in this article are solely those of the authors and do not necessarily represent those of their affiliated organizations, or those of the publisher, the editors and the reviewers. Any product that may be evaluated in this article, or claim that may be made by its manufacturer, is not guaranteed or endorsed by the publisher.

anticancer activity by inhibiting mitochondrial oxidative phosphorylation. ACS Appl. Mater Interfaces 14, 29521–29536. doi:10.1021/ACSAMI.2C05054

Biswas, A. (2021). Synthesis and characterization of about 20 nm Gold nanoparticles. Orient. J. Chem. 37, 1187–1191. doi:10.13005/ojc/370524

Cakaj, A., Lisiak-Zielińska, M., Hanć, A., Małecka, A., Borowiak, K., and Drapikowska, M. (2023). Common weeds as heavy metal bioindicators: a new approach in biomonitoring. *Sci. Rep.* 13, 1–14. doi:10.1038/s41598-023-34019-9

Cakaj, A., Drzewiecka, K., Hanć, A., Lisiak-Zielińska, M., Ciszewska, L., and Drapikowska, M. (2024). Plants as effective bioindicators for heavy metal pollution monitoring. *Environ. Res.* 256, 119222. doi:10.1016/j.envres.2024.119222

Camilo-Cotrim, C. F., Bailão, E. F. L. C., Ondei, L. S., Carneiro, F. M., and Almeida, L. M. (2022). What can the *Allium cepa* test say about pesticide safety? A review. *Environ. Sci. Pollut. Res.* 29, 48088–48104. doi:10.1007/s11356-022-20695-z

Carnerero, J. M., Sánchez-Coronilla, A., Jimenez-Ruiz, A., and Prado-Gotor, R. (2020). Factors that control the gold nanoparticles' aggregation induced by adenine molecules: new insights through a combined experimental and theoretical study. *J. Mol. Liq.* 310, 113136. doi:10.1016/j.molliq.2020.113136

Chang, M., Wang, H., Niu, J., Song, Y., and Zou, Z. (2020). Alkannin-induced oxidative DNA damage synergizes with PARP inhibition to cause cancer-specific cytotoxicity. *Front. Pharmacol.* 11, 610205. doi:10.3389/fphar.2020.610205

Clementi, E., Garajova, Z., and Markkanen, E. (2021). Measuring DNA damage using the alkaline comet assay in cultured cells. *Bio Protoc.* 11, e4119. doi:10.21769/BioProtoc.

Collins, A. R. (2002). The comet assay: principles, applications, and limitations. *Methods Mol. Biol.* 203, 163–177. doi:10.1385/1-59259-179-5:163

Collins, A. R., Oscoz, A. A., Brunborg, G., Gaivão, I., Giovannelli, L., Kruszewski, M., et al. (2008). The comet assay: topical issues. *Mutagenesis* 23, 143–151. doi:10.1093/mutage/gem051

Collins, A. R. (2017). The use of bacterial repair endonucleases in the comet assay. *Methods Mol. Biol.* 1641, 173–184. doi:10.1007/978-1-4939-7172-5_9

Collins, A., Møller, P., Gajski, G., Vodenková, S., Abdulwahed, A., Anderson, D., et al. (2023). Measuring DNA modifications with the comet assay: a compendium of protocols. *Nat. Protoc.* 18 (3 18), 929–989. doi:10.1038/s41596-022-00754-y

Copp, M. E., Chubinskaya, S., Bracey, D. N., Shine, J., Sessions, G., Loeser, R. F., et al. (2022). Comet assay for quantification of the increased DNA damage burden in primary human chondrocytes with aging and osteoarthritis. *Aging Cell* 21, e13698. doi:10.1111/acel.13698

Cordelli, E., Bignami, M., and Pacchierotti, F. (2021). Comet assay: a versatile but complex tool in genotoxicity testing. *Toxicol. Res.* (Camb) 10, 68–78. doi:10.1093/toxres/tfaa093

Darwish, H., Al-Osaimi, G. S., Al Kashgry, N. A. T., Sonbol, H., Alayafi, A. A. M., Alabdallah, N. M., et al. (2023). Evaluating the genotoxicity of salinity stress and secondary products gene manipulation in lime, citrus aurantifolia, plants. *Front. Plant Sci.* 14, 1211595. doi:10.3389/fpls.2023.1211595

De Berardis, B., Marchetti, M., Risuglia, A., Ietto, F., Fanizza, C., and Superti, F. (2020). Exposure to airborne gold nanoparticles: a review of current toxicological data on the respiratory tract. *J. Nanoparticle Res.* 22, 235–241. doi:10.1007/s11051-020-04966-9

Debnath, P., Mondal, A., Hajra, A., Das, C., and Mondal, N. K. (2018). Cytogenetic effects of silver and gold nanoparticles on *Allium cepa* roots. *J. Genet. Eng. Biotechnol.* 16, 519–526. doi:10.1016/j.jgeb.2018.07.007

Dhanapal, A. R., Thiruvengadam, M., Vairavanathan, J., Venkidasamy, B., Easwaran, M., and Ghorbanpour, M. (2024). Nanotechnology approaches for the remediation of agricultural polluted soils. *ACS Omega* 9, 13522–13533. doi:10.1021/acsomega.3c09776

Dheyab, M. A., Aziz, A. A., Jameel, M. S., Khaniabadi, P. M., and Oglat, A. A. (2020). Rapid sonochemically-assisted synthesis of highly stable gold nanoparticles as computed tomography contrast agents. *Appl. Sci.* 10, 7020–10. doi:10.3390/app10207020

DiPeso, L., Pendyala, S., Huang, H. Z., Fowler, D. M., and Hatch, E. M. (2025). Image-based identification and isolation of micronucleated cells to dissect cellular consequences [preprint]. *BioRxiv*, doi:10.1101/2023.05.04.539483

Djanaguiraman, M., Anbazhagan, V., Dhankher, O. P., and Prasad, P. V. V. (2024). Uptake, translocation, toxicity, and impact of nanoparticles on plant physiological processes. *Plants* 13, 3137. doi:10.3390/plants13223137

Donaldson, K., Tran, L., Jimenez, L. A., Duffin, R., Newby, D. E., Mills, N., et al. (2005). Combustion-derived nanoparticles: a review of their toxicology following inhalation exposure. *Part Fibre Toxicol.* 2, 10. doi:10.1186/1743-8977-2-10

Drzymała, J., and Kalka, J. (2024). Assessment of genotoxicity, mutagenicity, and cytotoxicity of diclofenac and sulfamethoxazole at environmental concentrations on *Vicia faba*. *Int. J. Environ. Sci. Technol.* 21, 3633–3648. doi:10.1007/s13762-023-05238-4

El Yamani, N., Rundén-Pran, E., Collins, A. R., Longhin, E. M., Elje, E., Hoet, P., et al. (2022). The miniaturized enzyme-modified comet assay for genotoxicity testing of nanomaterials. *Front. Toxicol.* 4, 986318. doi:10.3389/ftox.2022.986318

Ershov, B. G., Abkhalimov, E. V., Solovov, R. D., and Roldughin, V. I. (2016). Gold nanoparticles in aqueous solutions: influence of size and pH on hydrogen dissociative adsorption and au(iii) ion reduction. *Phys. Chem. Chem. Phys.* 18, 13459–13466. doi:10. 1039/C6CP01996J

Fathy, M. M., Elfiky, A. A., Bashandy, Y. S., Hamdy, M. M., Elgharib, A. M., Ibrahim, I. M., et al. (2023). An insight into synthesis and antitumor activity of citrate and gallate stabilizing gold nanospheres. *Sci. Rep.* 13 1–11. doi:10.1038/S41598-023-29821-4

Filippov, S. K., Khusnutdinov, R., Murmiliuk, A., Inam, W., Zakharova, L. Y., Zhang, H., et al. (2023). Dynamic light scattering and transmission electron microscopy in drug delivery: a roadmap for correct characterization of nanoparticles and interpretation of results. *Mater Horiz.* 10, 5354–5370. doi:10.1039/D3MH00717K

Frickenstein, A. N., Mukherjee, S., Harcourt, T., He, Y., Sheth, V., Wang, L., et al. (2023). Quantification of monodisperse and biocompatible gold nanoparticles by single-particle ICP-MS. *Anal. Bioanal. Chem.* 415, 4353–4366. doi:10.1007/s00216-023-04540-x

Fu, K., Wang, X., Yuan, X., Wang, D., Mi, X., Tan, X., et al. (2021). Size-dependent penetration of gold nanoprobes into fixed cells. $ACS\ Omega\ 6$, 3791–3799. doi:10.1021/acsomega.0c05458

Gharibkandi, N. A., Wawrowicz, K., Majkowska-Pilip, A., Żelechowska-Matysiak, K., Wierzbicki, M., and Bilewicz, A. (2023). Au@109Pd core–shell nanoparticle conjugated to trastuzumab for the therapy of HER2+ cancers: studies on the applicability of 109Pd/109mAg $in\ vivo$ generator in combined β – auger electron therapy. $EJNMMI\ Radiopharm.\ Chem.\ 8,\ 26–16.\ doi:10.1186/s41181-023-00212-4$

Giorgetti, L. (2019). Effects of nanoparticles in plants: phytotoxicity and genotoxicity assessment. nanomaterials in plants. Algae Microorg. Concepts Controv. 2, 65–87. doi:10.1016/B978-0-12-811488-9.00004-4

Girma, A. (2023). Alternative mechanisms of action of metallic nanoparticles to mitigate the global spread of antibiotic-resistant bacteria. *Cell Surf.* 10, 100112. doi:10. 1016/j.tcsw.2023.100112

Gojznikar, J., Zdravković, B., Vidak, M., Leskošek, B., and Ferk, P. (2022). TiO₂ nanoparticles and their effects on eukaryotic cells: a double-edged sword. *Int. J. Mol. Sci.* 23, 12353. doi:10.3390/ijms232012353

Gomes, A. M., Orr, B., Novais-Cruz, M., Sousa, F. D., Ferrás, C., Maiato, H., et al. (2022). Micronuclei from misaligned chromosomes that satisfy the spindle assembly checkpoint in cancer cells. *BioRxiv* 32, 4240–4254.e5. doi:10.1016/j.cub.2022.08.026

Ha, N., Seo, E., Kim, S., and Lee, S. J. (2021). Adsorption of nanoparticles suspended in a drop on a leaf surface of *Perilla frutescens* and their infiltration through stomatal pathway. *Sci. Rep.* 11 (1 11), 11556–13. doi:10.1038/s41598-021-91073-x

Han, M., Zhang, Z., Liu, S., Sheng, Y., Waigi, M. G., Hu, X., et al. (2023). Genotoxicity of organic contaminants in the soil: a review based on bibliometric analysis and methodological progress. *Chemosphere* 313, 137318. doi:10.1016/j.chemosphere.2022. 137318

Hernández-Saravia, L. P., Carmona, E. R., Villacorta, A., Carevic, F. S., and Marcos, R. (2023). Sustainable use of mining and electronic waste for nanomaterial synthesis with technological applications: state of the art and future directions. *Green Chem. Lett. Rev.* 16, 2260401. doi:10.1080/17518253.2023.2260401

Hu, D., Bai, Y., Li, L., Ai, M., Jin, J., Song, K., et al. (2022). Phytotoxicity assessment study of gold nanocluster on broad bean (*Vicia faba L.*) seedling. *Environ. Pollut. Bioavailab.* 34, 284–296. doi:10.1080/26395940.2022.2101543

Hwang, J. H. (2024). Toxicity assessment of a no-pain pharmacopuncture extract using a standard battery of *in vitro* chromosome aberration tests. *J. Pharmacopunct.* 27, 38–46. doi:10.3831/KPI.2024.27.1.38

Jiménez-Martínez, W. de J., Vázquez-Lira, J. C., Jiménez-Martínez, W. de J., and Vázquez-Lira, J. C. (2024). Una revisión de nanopartículas de oro: características fisicoquímicas y su respuesta celular en macrófagos. Mundo nano. *Rev. Interdiscip. Nanociencias Nanotecnología* 17, 1e–16e. (in Spanish). doi:10.22201/ceiich.24485691e.2024.33.69801

Kang, S., Rahman, A., McGinnis, S., and Vikesland, P. (2024). Toward environmentally favorable nano-sensing by production of reusable gold nanoparticles from gold nano-waste: life cycle and nanocircular economy implications. *Environ. Sci. Nano* 11, 1499–1507. doi:10.1039/D3EN00505D

Kato, T. A., and Haskins, J. S. (2023). Mitotic index analysis. *Methods Mol. Biol.* 2519, $17-26.\ doi:10.1007/978-1-0716-2433-3_3$

Khalid, H., Kashif Zahoor, M., Riaz, D., Arshad, M., Yaqoob, R., and Ranian, K. (2022). Sewage sludge-induced effect on growth, enzyme inhibition, and genotoxicity can be ameliorated using wheat straw and biochar in *Pheretima posthuma* earthworms. *Front. Environ. Sci.* 10, 888394. doi:10.3389/fenvs.2022.888394

Kim, S., Leem, J., Oh, J. S., and Kim, J. S. (2022). Cytotoxicity of 9,10-Phenanthrenequinone impairs mitotic progression and spindle assembly independent of ROS production in HeLa cells. *Toxics* 10, 327. doi:10.3390/toxics10060327

Klein, P., Chauvey, L., Kallerhoff, J., Pinelli, E., Morard, M., and Silvestre, J. (2021). A tool derived from the *Vicia faba* micronucleus assay, to assess genotoxicity, cytotoxicity or biostimulation of novel compounds used in agriculture. *Agronomy* 11, 321. doi:10. 3390/agronomy11020321

Kumah, E. A., Fopa, R. D., Harati, S., Boadu, P., Zohoori, F. V., and Pak, T. (2023). Human and environmental impacts of nanoparticles: a scoping review of the current literature. *BMC Public Health* 23 (1 23), 1059–28. doi:10.1186/s12889-023-15958-4

Kumari, S., Raturi, S., Kulshrestha, S., Chauhan, K., Dhingra, S., András, K., et al. (2023). A comprehensive review on various techniques used for synthesizing nanoparticles. *J. Mater. Res. Technol.* 27, 1739–1763. doi:10.1016/j.jmrt.2023.09.291

Kuznetsova, E. V., Kuznetsov, N. M., Kalinin, K. T., Lebedev-Stepanov, P. V., Novikov, A. A., and Chvalun, S. N. (2022). The role of integrated approach in the determination of nanoparticle sizes in dispersions. *Colloid J.* 84, 704–714. doi:10.1134/s1061933x22600348

Landsiedel, R., Honarvar, N., Seiffert, S. B., Oesch, B., and Oesch, F. (2022). Genotoxicity testing of nanomaterials. Wiley Interdiscip. Rev. Nanomed Nanobiotechnol 14, e1833. doi:10.1002/wnan.1833

Lebedová, J., Hedberg, Y. S., Odnevall Wallinder, I., and Karlsson, H. L. (2018). Size-dependent genotoxicity of silver, gold and platinum nanoparticles studied using the mini-gel comet assay and micronucleus scoring with flow cytometry. *Mutagenesis* 33, 77–85. doi:10.1093/mutage/gex027

Leem, J., Kim, S., Kim, J. S., and Oh, J. S. (2022). ROS-Independent cytotoxicity of 9,10-phenanthrenequinone inhibits cell cycle progression and spindle assembly during meiotic maturation in mouse oocytes. *J. Hazard Mater* 436, 129248. doi:10.1016/j. ihazmat.2022.129248

Lespes, G., Faucher, S., and Slaveykova, V. I. (2020). Natural nanoparticles, anthropogenic nanoparticles, where is the frontier? *Front. Environ. Sci.* 8, 71. doi:10. 3389/fenvs.2020.00071

Li, J. J., Hartono, D., Ong, C. N., Bay, B. H., and Yung, L. Y. L. (2010). Autophagy and oxidative stress associated with gold nanoparticles. *Biomaterials* 31, 5996–6003. doi:10. 1016/i.biomaterials.2010.04.014

Li, Q., Huang, C., Liu, L., Hu, R., and Qu, J. (2018a). Effect of surface coating of gold nanoparticles on cytotoxicity and cell cycle progression. *Nanomaterials* 8, 1063. doi:10. 3390/NANO8121063

Li, Q., Huang, C., Liu, L., Hu, R., and Qu, J. (2018b). Effect of surface coating of gold nanoparticles on cytotoxicity and cell cycle progression. *Nanomaterials* 8, 1063. doi:10. 3390/nano8121063

Li, J., Carlson, B. E., Yung, Y. L., Lv, D., Hansen, J., Penner, J. E., et al. (2022). Scattering and absorbing aerosols in the climate system. *Nat. Rev. Earth Environ.* 3 (6 3), 363–379. doi:10.1038/s43017-022-00296-7

Li, X., Li, A., Zhang, M., and Gao, T. (2023). Cytotoxicity and genotoxicity evaluation of chloroform using *Vicia faba* roots. *Toxicol. Ind. Health* 39, 603–612. doi:10.1177/07482337231191573

Liman, R., Ali, M. M., İstifli, E. S., Ciğerci, İ. H., Tınaz, Ü., Kırlangıç, S., et al. (2025). Cyto-genotoxic assessment of sulfoxaflor in *Allium cepa* root cells and DNA docking studies. *Microsc. Res. Tech.* 88, 1521. 1533. doi:10.1002/jemt.24807

Lin, W., Zhang, W., Paterson, G. A., Zhu, Q., Zhao, X., Knight, R., et al. (2020). Expanding magnetic organelle biogenesis in the domain bacteria. *Microbiome* 8, 152. doi:10.1186/s40168-020-00931-9

Liu, X., Atwater, M., Wang, J., Dai, Q., Zou, J., Brennan, J. P., et al. (2007). A study on gold nanoparticle synthesis using oleylamine as both reducing agent and protecting ligand. *J. Nanosci. Nanotechnol.* 7, 3126–3133. doi:10.1166/jnn.2007.805

Liu, Y., Yuan, H., Wang, H., and Wang, Z. (2021). *In situ* transmission electron microscopy investigation of melting/evaporation kinetics in anisotropic gold nanoparticles. *Materials* 14, 7332. doi:10.3390/ma14237332

López-Moreno, M. L., de la Rosa, G., Cruz-Jiménez, G., Castellano, L., Peralta-Videa, J. R., and Gardea-Torresdey, J. L. (2017). Effect of ZnO nanoparticles on corn seedlings at different temperatures; X-ray absorption spectroscopy and ICP/OES studies. *Microchem. J.* 134, 54–61. doi:10.1016/j.microc.2017.05.007

Lotze, M. T., Lu, L., and Taylor, D. L. (2004). Imaging cytometry: high content screening for large-scale cell research. *Meas. Immun. Basic Sci. Clin. Pract.*, 660–665. doi:10.1016/B978-012455900-4/50320-2

Lu, Y., Ma, Q., Xu, X., Yu, Z., Guo, T., and Wu, Y. (2021). Retracted: cytotoxicity and genotoxicity evaluation of polystyrene microplastics on *Vicia faba* roots. *Environ. Pollut.* 288, 117821. doi:10.1016/j.envpol.2021.117821

- Ma, T. H., Xu, Z., Xu, C., McConnell, H., Valtierra Rabago, E., Adriana Arreola, G., et al. (1995). The improved Allium/Vicia root tip micronucleus assay for clastogenicity of environmental pollutants. *Mutat. Research/Environ. Mutagen. Relat. Subj.* 334, 185–195. doi:10.1016/0165-1161(95)90010-1
- Madnay, M. M. Y., Obaid, W. A., Selim, S., Mohamed Reyad, A., Alsherif, E. A., Korany, S. M., et al. (2022). Rhodospirillum sp. JY3: an innovative tool to mitigate the phytotoxic impact of galaxolide on wheat (*Triticum aestivum*) and faba bean (*Vicia faba*) plants. Front. Plant Sci. 13, 1037474. doi:10.3389/fpls.2022.1037474
- Maguire, C. M., Rösslein, M., Wick, P., and Prina-Mello, A. (2018). Characterisation of particles in solution a perspective on light scattering and comparative technologies. *Sci. Technol. Adv. Mater* 19, 732–745. doi:10.1080/14686996.2018.1517587
- Malik, S., Muhammad, K., and Waheed, Y. (2023). Nanotechnology: a revolution in modern industry. *Molecules* 28, 661. doi:10.3390/molecules28020661
- Mammari, N., Lamouroux, E., Boudier, A., and Duval, R. E. (2022). Current knowledge on the oxidative-stress-mediated antimicrobial properties of metal-based nanoparticles. *Microorganisms* 10, 437. doi:10.3390/microorganisms10020437
- Martínez, G., Merinero, M., Pérez-Aranda, M., Pérez-Soriano, E. M., Ortiz, T., Begines, B., et al. (2020). Environmental impact of nanoparticles' application as an emerging technology: a review. *Materials* 14, 166. doi:10.3390/ma14010166
- Mat Lazim, Z., Salmiati, S., Marpongahtun, M., Arman, N. Z., Mohd Haniffah, M. R., Azman, S., et al. (2023). Distribution of silver (Ag) and silver nanoparticles (AgNPs) in aquatic environment. *Water* 15, 1349. doi:10.3390/w15071349
- Mekuye, B., and Abera, B. (2023). Nanomaterials: an overview of synthesis, classification, characterization, and applications. *Nano Sel.* 4, 486–501. doi:10.1002/nano.202300038
- Melo, L., Hui, A., Kowal, M., Boateng, E., Poursorkh, Z., Rocheron, E., et al. (2021). Size distributions of gold nanoparticles in solution measured by single-particle mass photometry. *J. Phys. Chem. B* 125, 12466–12475. doi:10.1021/acs.jpcb.1c05557
- Mgadi, K., Ndaba, B., Roopnarain, A., Rama, H., and Adeleke, R. (2024). Nanoparticle applications in agriculture: overview and response of plant-associated microorganisms. *Front. Microbiol.* 15, 1354440. doi:10.3389/fmicb.2024.1354440
- Mironava, T., Hadjiargyrou, M., Simon, M., Jurukovski, V., and Rafailovich, M. H. (2010). Gold nanoparticles cellular toxicity and recovery: effect of size, concentration and exposure time. *Nanotoxicology* 4, 120–137. doi:10.3109/17435390903471463
- Mitra, S., and Chattopadhyay, A. K. (2013). Determination of potassium dichromateinduced genotoxicity by using higher plant bioassay system. *International Journal of Current Life Sciences* 3, 272–275.
- Møller, P., Azqueta, A., Boutet-Robinet, E., Milić, M., Collins, A., Langie, S. A. S., et al. (2020). Minimum information for reporting on the comet assay (MIRCA): recommendations for describing comet assay procedures and results. *Nat. Protoc.* 15, 3817–3826. doi:10.1038/s41596-020-0398-1
- Neme, A., Leta, A., Yones, A. M., and Tahir, M. (2023). Seedborne mycoflora of faba bean (*Vicia fabae* L.) and evaluation of plant extract and Trichoderma species against mycelium growth of selected fungi. *Heliyon* 9, e17291. doi:10.1016/j.heliyon.2023.e17291
- Nirmala, J. G., and Lopus, M. (2019). Tryptone-stabilized gold nanoparticles induce unipolar clustering of supernumerary centrosomes and G1 arrest in triple-negative breast cancer cells. *Sci. Rep.* 9 (19), 19126–11. doi:10.1038/s41598-019-55555-3
- Niżnik, Ł., Noga, M., Kobylarz, D., Frydrych, A., Krośniak, A., Kapka-Skrzypczak, L., et al. (2024). Gold nanoparticles (AuNPs)—Toxicity, safety and green synthesis: a critical review. *Int. J. Mol. Sci.* 25, 4057. doi:10.3390/IJMS25074057
- OECD (2016). Test No. 473: In Vitro Mammalian Chromosomal Aberration Test. Paris: OECD Publishing. doi:10.1787/9789264264649-en
- Oliveira, A. E. F., Pereira, A. C., Resende, M. A. C., Ferreira, L. F., Elisa, A., Oliveira, F., et al. (2023). Gold nanoparticles: a didactic step-by-step of the synthesis using the turkevich method, mechanisms, and characterizations. *Analytica* 4, 250–263. doi:10. 3390/analytica4020020
- Onisan, E., Sarac, I., Petolescu, C., Horablaga, M. N., Mate, C., Simina, A., et al. (2025). Application of the allium test in toxicity studies of lead and copper: a cytological perspective. *Appl. Sci.* 15, 1491. doi:10.3390/app15031491
- Owolarafe, T. A., Salawu, K., Ihegboro, G. O., Ononamadu, C. J., Alhassan, A. J., and Wudil, A. M. (2020). Investigation of cytotoxicity potential of different extracts of *Ziziphus mauritiana* (Lam) leaf *Allium cepa* model. *Toxicol. Rep.* 7, 816. 821. doi:10. 1016/j.toxrep.2020.06.010
- Pan, Y., Neuss, S., Leifert, A., Fischler, M., Wen, F., Simon, U., et al. (2007). Size-dependent cytotoxicity of gold nanoparticles. *Small* 3, 1941–1949. doi:10.1002/smll. 200700378
- Pan, Y., Leifert, A., Ruau, D., Neuss, S., Bornemann, J., Schmid, G., et al. (2009). Gold nanoparticles of diameter 1.4 nm trigger necrosis by oxidative stress and mitochondrial damage. *Small* 5, 2067–2076. doi:10.1002/smll.200900466
- Pang, Y. T., Ge, Z., Zhang, B., Xiu, P., Li, Q., and Wang, Y. (2020). Pore formation induced by nanoparticles binding to a lipid membrane. *Nanoscale* 12, 7902–7913. doi:10.1039/C9NR10534D
- Patel, K. N., Trivedi, P. G., Thakar, M. S., Prajapati, K. V., Prajapati, D. K., and Sindhav, G. M. (2023). Gold nanoparticles synthesis using *Gymnosporia montana* L.

and its biological profile: a pioneer report. *J. Genet. Eng. Biotechnol.* 21, 71. doi:10.1186/s43141-023-00525-6

- Patlolla, A. K., Barnes, C., Hackett, D., and Tchounwou, P. B. (2009). Potassium dichromate induced cytotoxicity, genotoxicity and oxidative stress in human liver carcinoma (HepG2) cells. *Int. J. Environ. Res. Public Health* 6, 643–653. doi:10.3390/ijerph6020643
- Polechońska, L., and Klink, A. (2023). Macrophytes as passive bioindicators of trace element pollution in the aquatic environment. *Wiley Interdiscip. Rev. Water* 10, e1630. doi:10.1002/wat2.1630
- Portugal, J., Bedia, C., Amato, F., Juárez-Facio, A. T., Stamatiou, R., Lazou, A., et al. (2024). Toxicity of airborne nanoparticles: facts and challenges. *Environ. Int.* 190, 108889. doi:10.1016/j.envint.2024.108889
- Pourali, P., and Benson, V. (2025). Cellular delivery of functional AntimiR conjugated to bio-produced gold nanoparticles. *Non-Coding RNA* 11, 66. doi:10.3390/NCRNA11050066
- Pourali, P., Benada, O., Pátek, M., Neuhöoferová, E., Dzmitruk, V., and Benson, V. (2021). Response of biological gold nanoparticles to different pH values: is it possible to prepare both negatively and positively charged nanoparticles? *Appl. Sci.* 11, 11559. doi:10.3390/app112311559
- Rajeshwari, A., Suresh, S., Chandrasekaran, N., and Mukherjee, A. (2016). Toxicity evaluation of gold nanoparticles using an *Allium cepa* bioassay. *RSC Adv.* 6, 24000–24009. doi:10.1039/C6RA04712B
- Ramalingam, V., Revathidevi, S., Shanmuganayagam, T., Muthulakshmi, L., and Rajaram, R. (2016). Biogenic gold nanoparticles induce cell cycle arrest through oxidative stress and sensitize mitochondrial membranes in A549 lung cancer cells. *RSC Adv.* 6, 20598–20608. doi:10.1039/C5RA26781A
- Reipa, V., Hackley, V. A., Tona, A., Heo, M. B., Lee, Y. R., Lee, T. G., et al. (2025). Well-characterized polyethyleneimine-/carboxylated-polyethylene-glycol-functionalized gold nanoparticles as prospective nanoscale control materials for in vitro cell viability assays: particle characterization and toxicity tests in eight mammalian cell lines. Nanomaterials 15, 79. doi:10.3390/nano15020079
- Romero-Freire, A., González, V., Groenenberg, J. E., Qiu, H., Auffan, M., Cotelle, S., et al. (2021). Cytotoxicity and genotoxicity of lanthanides for *Vicia faba L.* are mediated by their chemical speciation in different exposure media. *Sci. Total Environ.* 790, 148223. doi:10.1016/j.scitotenv.2021.148223
- Roy, S. G. (2022). A review of plant bioindicators in wetlands. Adv. Environ. Eng. Res. 3 (052 3), 1–12. doi:10.21926/aeer.2204052
- Rudolf, R., Majerič, P., Jelen, Z., Horvat, A., and Krajnc, D. (2024a). The environmental impact of using gold nanoparticles and 3HFWC in cosmetics, as determined with LCA methodology. *Rev. Inorg. Chem.* 44, 409–419. doi:10.1515/revic-2024-0012
- Rudolf, R., Majerič, P., Pintarič, Z. N., Horvat, A., and Krajnc, D. (2024b). Life cycle assessment (LCA) of the impact on the environment of a cosmetic cream with gold nanoparticles and hydroxylated fullerene ingredients. *Appl. Sci.* 14, 11625. doi:10.3390/app142411625
- Saidi, D., Obeidat, M., Alsotari, S., Ibrahim, A. A., Al-Buqain, R., Wehaibi, S., et al. (2024). Formulation optimization of lyophilized aptamer-gold nanoparticles: maintained colloidal stability and cellular uptake. *Heliyon* 10, e30743. doi:10.1016/j. heliyon.2024.e30743
- Sani, A., Cao, C., and Cui, D. (2021). Toxicity of gold nanoparticles (AuNPs): a review. *Biochem. Biophys. Rep.* 26, 100991. doi:10.1016/j.bbrep.2021.100991
- Sanità, G., Carrese, B., and Lamberti, A. (2020). Nanoparticle surface functionalization: how to improve biocompatibility and cellular internalization. *Front. Mol. Biosci.* 7, 587012. doi:10.3389/fmolb.2020.587012
- Santhoshkumar, J., Rajeshkumar, S., and Venkat Kumar, S. (2017). Phyto-assisted synthesis, characterization and applications of gold nanoparticles a review. *Biochem. Biophys. Rep.* 11, 46–57. doi:10.1016/j.bbrep.2017.06.004
- Santibáñez-Andrade, M., Sánchez-Pérez, Y., Chirino, Y. I., Morales-Bárcenas, R., Quintana-Belmares, R., and García-Cuellar, C. M. (2022). Particulate matter (PM10) destabilizes mitotic spindle through downregulation of SETD2 in A549 lung cancer cells. *Chemosphere* 295, 133900. doi:10.1016/j.chemosphere.2022.133900
- Sarsar, O., Kalefetoğlu Macar, T., Çavuşoğlu, K., Yalçın, E., and Acar, A. (2025). Multifaceted investigation of esfenvalerate-induced toxicity on *Allium cepa L. Sci. Rep.* 15 (1 15), 16977–17. doi:10.1038/s41598-025-01638-3
- Sembada, A. A., and Lenggoro, I. W. (2024). Transport of nanoparticles into plants and their detection methods. *Nanomaterials* 14, 131–14. doi:10.3390/nano14020131
- Serrano Ortíz, R. M., Estrella Parra, E. A., Alarcón Herrera, N., and Flores Maya, S. (2024). Determinación del efecto genotóxico o antigenotóxico de extractos de semillas de Malus domestica, mediante la prueba de ensayo de micronúcleos en raíces de *Vicia faba. Biocyt Biol. Cienc. Tecnol.* 17 (1), 1220–1228. (in Spanish). doi:10.22201/fesi. 20072082e.2024.17.85897
- Shukla, R. K., Sharma, V., Pandey, A. K., Singh, S., Sultana, S., and Dhawan, A. (2011). ROS-mediated genotoxicity induced by titanium dioxide nanoparticles in human epidermal cells. *Toxicol. Vitro* 25, 231–241. doi:10.1016/j.tiv.2010.11.008
- Siddiqi, K. S., and Husen, A. (2017). Plant response to engineered metal oxide nanoparticles. *Nanoscale Res. Lett.* 12, 92. doi:10.1186/S11671-017-1861-Y

Sieprawska, A., Rudolphi-Szydło, E., Skórka, M., Telk, A., and Filek, M. (2024). Assessment of the oxidative stress intensity and the integrity of cell membranes under the manganese nanoparticles toxicity in wheat seedlings. *Sci. Rep.* 14, 1–10. doi:10.1038/s41598-024-53697-7

Sommer, S., Buraczewska, I., and Kruszewski, M. (2020). Micronucleus assay: the state of art, and future directions. *Int. J. Mol. Sci.* 21, 1534. doi:10.3390/ijms21041534

Song, J., Kim, D., and Lee, D. (2011). Size control in the synthesis of 1-6 nm gold nanoparticles *via* solvent-controlled nucleation. *Langmuir* 27, 13854–13860. doi:10.1021/la203113r

Sousa De Almeida, M., Susnik, E., Drasler, B., Taladriz-Blanco, P., Petri-Fink, A., and Rothen-Rutishauser, B. (2021). Understanding nanoparticle endocytosis to improve targeting strategies in nanomedicine. *Chem. Soc. Rev.* 50, 5397–5434. doi:10.1039/D0CS01127D

Štefanić, P. P., Košpić, K., Lyons, D. M., Jurković, L., Balen, B., and Tkalec, M. (2021). Phytotoxicity of silver nanoparticles on tobacco plants: evaluation of coating effects on photosynthetic performance and chloroplast ultrastructure. *Nanomaterials* 11, 744. doi:10.3390/nano11030744

Sukhanova, A., Bozrova, S., Sokolov, P., Berestovoy, M., Karaulov, A., and Nabiev, I. (2018). Dependence of nanoparticle toxicity on their physical and chemical properties. *Nanoscale Res. Lett.* 13 (1 13), 1–21. doi:10.1186/S11671-018-2457-X

Tang, Y., Zhao, W., Zhu, G., Tan, Z., Huang, L., Zhang, P., et al. (2023). Nanopesticides and fertilizers: solutions for global food security. *Nanomaterials* 14, 90. doi:10. 3300/nanol4010090

Teles, M. (2019). L'exposició a les nanopartícules d'or modula l'expressió de gens immunes innats i antioxidants en la Dorada. Barcelona: Universitat Autònoma de Barcelona (UAB Divulga), 0001-0003.

Toscano, F., and Torres-Arias, M. (2023). Nanoparticles cellular uptake, trafficking, activation, toxicity and *in vitro* evaluation. *Curr. Res. Immunol.* 4, 100073. doi:10.1016/j.crimmu.2023.100073

Tsai, S. W., Lo, C. Y., Yu, S. Y., Chen, F. H., Huang, H. C., Wang, L. K., et al. (2022). Gold nanoparticles enhancing generation of ROS for Cs-137 radiotherapy. *Nanoscale Res. Lett.* 17, 123–129. doi:10.1186/s11671-022-03761-w

Üstündağ, Ü., Macar, O., Kalefetoğlu Macar, T., Yalçın, E., and Çavuşoğlu, K. (2023). Effect of *Melissa officinalis* L. leaf extract on manganese-induced cyto-genotoxicity on *Allium cepa* L. *Sci. Rep.* 13, 22110–22114. doi:10.1038/s41598-023-49699-6

Uyeki, E. M., Nishio, A., and Uyeki, E. M. (1983). Antiproliferative and genotoxic effects of chromium on cultured mammalian cells. *J. Toxicol. Environ. Health, Part A Curr. Issues* 11, 227–235. doi:10.1080/15287398309530337

Vales, G., Suhonen, S., Siivola, K. M., Savolainen, K. M., Catalán, J., and Norppa, H. (2020). Genotoxicity and cytotoxicity of gold nanoparticles *in vitro*: role of surface functionalization and particle size. *Nanomaterials* 10, 271. doi:10.3390/nano10020271

Vallabani, N. V. S., and Karlsson, H. L. (2022). Primary and secondary genotoxicity of nanoparticles: establishing a co-culture protocol for assessing micronucleus using flow cytometry. *Front. Toxicol.* 4, 845987. doi:10.3389/ftox.2022.845987

Velumani, P., Palani, N., Antalin Casmie, A., Senthilvel, R., and Parthasarthy, V. (2025). Cellular and chromosomal interaction of bio-synthesized copper oxide nanoparticles - induced nano-cytotoxicity and genotoxicity. *Toxicol. Vitro* 104, 106000. doi:10.1016/i.tiv.2024.106000

Wang, Y., Zhang, H., Shi, L., Xu, J., Duan, G., and Yang, H. (2020). A focus on the genotoxicity of gold nanoparticles. *Nanomedicine* 15, 319–323. doi:10.2217/NNM-2019-0364

Wang, F., Zhou, L., Mu, D., Zhang, H., Zhang, G., Huang, X., et al. (2024). Current research on ecotoxicity of metal-based nanoparticles: from exposure pathways, ecotoxicological effects to toxicity mechanisms. *Front. Public Health* 12, 1390099. doi:10.3389/fpubh.2024.1390099

Wang, J., Giordani, S., Marassi, V., Placci, A., Roda, B., Reschiglian, P., et al. (2024). Multi-environment and multi-parameter screening of stability and coating efficiency of

gold nanoparticle bioconjugates in application media. Sci. Rep. 14, 1–11. doi:10.1038/S41598-024-73624-0

Warnasuriya, S. D., Udayanga, D., Manamgoda, D. S., and Biles, C. (2023). Fungi as environmental bioindicators. *Sci. Total Environ.* 892, 164583. doi:10.1016/j.scitotenv. 2023.164583

Warr, T. J., Parry, E. M., and Parry, J. M. (1993). A comparison of two *in vitro* mammalian cell cytogenetic assays for the detection of mitotic aneuploidy using 10 known or suspected aneugens. *Mutat. Research/Fundamental Mol. Mech. Mutagen.* 287, 29–46. doi:10.1016/0027-5107(93)90143-4

Warsame, A. O., O'Sullivan, D. M., and Tosi, P. (2018). Seed storage proteins of faba bean (*Vicia faba* L): current status and prospects for genetic improvement. *J. Agric. Food Chem.* 66, 12617–12626. doi:10.1021/acs.jafc.8b04992

Woźniak, A., Malankowska, A., Nowaczyk, G., Grześkowiak, B. F., Tuśnio, K., Słomski, R., et al. (2017). Size and shape-dependent cytotoxicity profile of gold nanoparticles for biomedical applications. *J. Mater Sci. Mater Med.* 28, 92. doi:10. 1007/S10856-017-5902-Y

Wypij, M., Jędrzejewski, T., Trzcińska-Wencel, J., Ostrowski, M., Rai, M., and Golińska, P. (2021). Green synthesized silver nanoparticles: antibacterial and anticancer activities, biocompatibility, and analyses of surface-attached proteins. *Front. Microbiol.* 12, 632505. doi:10.3389/fmicb.2021.632505

Xia, Q., Li, H., Liu, Y., Zhang, S., Feng, Q., and Xiao, K. (2017). The effect of particle size on the genotoxicity of gold nanoparticles. *J. Biomed. Mater Res. A* 105, 710–719. doi:10.1002/JBM.A.35944

Xia, Q., Huang, J., Feng, Q., Chen, X., Liu, X., Li, X., et al. (2019). Size- and cell type-dependent cellular uptake, cytotoxicity and *in vivo* distribution of gold nanoparticles. *Int. J. Nanomedicine* 14, 6957–6970. doi:10.2147/IJN.S214008

Xiong, C., Li, J., Liu, Z., and Zhang, Z. (2022). The dominant role of aerosol-cloud interactions in aerosol-boundary layer feedback: case studies in three megacities in China. *Front. Environ. Sci.* 10, 1002412. doi:10.3389/fenvs.2022.1002412

Yang, W., Guo, Y., Li, Y., Zheng, Y., Dong, K., and Dong, Y. (2022). Cinnamic acid toxicity on the structural resistance and photosynthetic physiology of Faba bean promoted the occurrence of fusarium wilt of Faba bean, which was alleviated through wheat and Faba bean intercropping. *Front. Plant Sci.* 13, 857780. doi:10. 3389/fbls.2022.857780

Yoon, J. H., Kim, J. K., Eun, J. W., Ashktorab, H., Smoot, D. T., Nam, S. W., et al. (2025). NKX6.3 modulation of mitotic dynamics and genomic stability in gastric carcinogenesis. *Cell Commun. Signal* 23, 35. doi:10.1186/s12964-025-02030-4

Yu, Z., Xu, X., Guo, L., Jin, R., and Lu, Y. (2024). Uptake and transport of micro/nanoplastics in terrestrial plants: detection, mechanisms, and influencing factors. *Sci. Total Environ.* 907, 168155. doi:10.1016/j.scitotenv.2023.168155

Zahra, Z., Habib, Z., Hyun, S., and Sajid, M. (2022). Nanowaste: another future waste, its sources, release mechanism, and removal strategies in the environment. Sustainability 14, 2041. doi:10.3390/su14042041

Zarnescu, -E., Jung, M. C., Ristea, M.-E., and Zarnescu, O. (2024). Effects of indigo carmine on growth, cell division, and morphology of *Allium cepa* L. root tip. *Toxics* 12, 194. doi:10.3390/toxics12030194

Zaveri, R. A., Wang, J., Fan, J., Zhang, Y., Shilling, J. E., Zelenyuk, A., et al. (2022). Rapid growth of anthropogenic organic nanoparticles greatly alters cloud life cycle in the Amazon rainforest. *Sci. Adv.* 8, eabj0329. doi:10.1126/sciadv.abj0329

Zhang, S., and Wang, C. (2023). Precise analysis of nanoparticle size distribution in TEM image. $Methods\ Protoc.\ 6,\ 63.\ doi:10.3390/mps6040063$

Zhang, L., Ma, Y., Wei, Z., and Wang, L. (2024). Toxicity of gold nanoparticles complicated by the co-existence multiscale plastics. *Front. Microbiol.* 15, 1447046. doi:10.3389/fmicb.2024.1447046

Zhou, X., El-Sappah, A. H., Khaskhoussi, A., Huang, Q., Atif, A. M., Elhamid, M. A. A., et al. (2024). Nanoparticles: a promising tool against environmental stress in plants. *Front. Plant Sci.* 15, 1509047. doi:10.3389/fpls.2024.1509047